Numerical investigation of efficiency loss mechanisms in light emitting diodes and determination of radiative and non-radiative lifetimes for infrared optoelectronics

(Article begins on next page)

04 August 2020

Numerical investigation of efficiency loss mechanisms in light emitting diodes and determination of radiative and non-radiative lifetimes for infrared optoelectronics

Stefano Dominici

Ph.D. Electronic Engineering
XXIX cycle

Dipartimento di Elettronica e Telecomunicazioni
Politecnico di Torino

Supervisor	Francesco Bertazzi
Co-Supervisor	Michele Goano
Examination Committee	Enrico Bellotti
	Pierluigi Debernardi
	Aldo Di Carlo
	Gianluca Fiori
	Åsa Haglund

Al mattino presto, il morale è più alto.
Durante il giorno s'abbassa.
A sera i pensieri volano a casa.

— *Sun Tzu*

Abstract

The year 2015 was defined the *international year of light* and light-based technologies. This title did not come unexpected, the research activity in solid-state lighting intensified during the last decade striving to improve solid-state light sources in terms of power consumption and fabrication costs. Emerging technologies are going to improve and amplify the scope of applicability of current solid-state lighting technology.

This work would like to give a contribution to scientific research in solid-state lighting on two fronts. First, by contributing to the determination of the optical properties of germanium and germanium-tin alloy and second, by searching for remedies to the temperature dependent efficiency loss in GaN/InGaN based blue light emitting diodes.

On these premises, this work has been splitted in two parts. In part one, the Auger recombination properties of germanium and radiative and Auger recombination properties for germanium-tin alloy have been calculated. In case of germanium, the application of a minimum biaxial tensile strain turns the material to a direct gap semiconductor, suitable for active and passive optoelectronic applications. On the other hand, the germanium-tin alloy is even more interesting due to its tunable band-gap energy and the capability to turn into a direct gap material above a certain molar fraction. On top of that, both materials may represent cheaper alternatives to materials currently used for the fabrication of high performance photodetectors and active optoelectronic devices. For both materials, the Auger and radiative recombination properties have been determined through a novel numerical approach that applies a Green's function based model to the full band structure of the material.

In part two, the temperature dependent efficiency loss, experimentally detected in a reference GaN/InGaN based single quantum well light emitting diode, has been numerically studied by measn of a commercial simulation software Crosslight APSYS©. The charge transport mechanism in the device has been modeled through an improved drift-diffusion scheme and compared to the real device current-voltage characteristics. Once an agreement between real and simulated current-voltage characteristics was achieved, the impact of Shockley-Read-Hall recombination mechanism on the device internal quantum efficiency function of temperature has been throughfully studied.

Publications

[1] F. Bertazzi, S. Dominici, M. Mandurrino, D. Robidas, X. Zhou, M. Vallone, M. Calciati, P. Debernardi, G. Verzellesi, M. Meneghini, E. Bellotti, G. Ghione, and M. Goano. "Modeling challenges for high-efficiency visible light-emitting diodes." In: *Research and Technologies for Society and Industry Leveraging a better tomorrow (RTSI), 2015 IEEE 1st International Forum on.* 2015, pp. 157–160. DOI: 10.1109/RTSI.2015.7325090.

[2] C. De Santi, M. Meneghini, M. La Grassa, B. Galler, R. Zeisel, M. Goano, S. Dominici, M. Mandurrino, F. Bertazzi, G. Meneghesso, and E. Zanoni. "Investigation of the thermal droop in InGaN-layers and blue LEDs." In: *International workshop on nitride semiconductors.* 2016.

[3] C. De Santi, M. Meneghini, M. La Grassa, B. Galler, R. Zeisel, M. Goano, S. Dominici, M. Mandurrino, F. Bertazzi, D. Robidas, et al. "Role of defects in the thermal droop of InGaN-based light emitting diodes." In: *Journal of Applied Physics* 119.9 (2016), p. 094501. DOI: 10.1063/1.4942438.

[4] S. Dominici, H. Wen, F. Bertazzi, M. Goano, and E. Bellotti. "Numerical evaluation of Auger recombination coefficients in relaxed and strained germanium." In: *Applied Physics Letters* 108.21 (2016), p. 211103. DOI: 10.1063/1.4952720.

[5] S. Dominici, H. Wen, B. Francesco, G. Michele, and B. Enrico. "Numerical study on the optical and carrier recombination processes in GeSn alloy for E-SWIR and MWIR optoelectronic applications." In: *Optics Express* 24.23 (2016), pp. 26363–26381. DOI: 10.1364/OE.24.026363.

[6] A. Glasmann, S. Dominici, W. Hanqing, and E. Bellotti. "Auger and Radiative Lifetimes in ESWIR Materials: HgCdTe, InGaAs, and GeSn." In: *II-VI Workshop.* 2016.

[7] M. Goano, F. Bertazzi, X. Zhou, M. Mandurrino, S. Dominici, M. Vallone, G. Ghione, F. Dolcini, F. Rossi, G. Verzellesi, M. Meneghini, E. Zanoni, and E. Bellotti. "Challenges towards the simulation of GaN-based LEDs beyond the semiclassical framework (invited)." In: *SPIE Photonics West, Light-Emitting Diodes: Materials, Devices, and Applications for Solid State Lighting XX.* 2016. DOI: 10.1117/12.2216489.

[8] M. Mandurrino, G. Verzellesi, M. Goano, S. Dominci, F. Bertazzi, G. Ghione, M. Meneghini, G. Meneghesso, and E. Zanoni. "Defect-related tunneling contributions to subthreshold forward current in GaN-based LEDs." In: *Fotonica 2015 AEIT*. 2015. DOI: 10.1049/cp.2015.0136.

[9] M. Mandurrino, M. Goano, S. Dominici, M. Vallone, F. Bertazzi, G. Ghione, L. Bernabei, L. Rovati, G. Verzellesi, M. Meneghini, G. Meneghesso, and E. Zanoni. "Trap-assisted tunneling contributions to subthreshold forward current in In- GaN/GaN light-emitting diodes." In: *SPIE Optics+Photonics, 14th International Conference on Solid State Lighting and LED-based Illumination Systems*. 2015. DOI: 10.1117/12.2187443.

[10] M. Meneghini, C. De Santi, M. La Grassa, B. Galler, R. Zeisel, B. Hahn, M. Goano, S. Dominici, M. Mandurrino, F. Bertazzi, G. Meneghesso, and E. Zanoni. "Thermal droop in InGaN-based LEDs: physical origin and dependence on material properties." In: *SPIE Photonics West, Light-Emitting Diodes: Materials, Devices, and Applications for Solid State Lighting XX*. 2016. DOI: 10.1117/12.2210953.

Acknowledgments

General Introduction

In recent years, the scientific research on optoelectronic devices, especially for commercial and military applications, invested resources to improve the efficiency of already existing devices and to study novel materials. Due to the importance of illumination systems in everyday life, the lighting industry soared leaps and bounds during the past decade. From historical illumination systems such as incandescent bulbs and sodium lamps, humankind has nowday entered the solid-state lighting era. Solid-state lighting devices, not only substituted outdated illumination systems, become part of everyday life through computers, communication devices, and entertainment systems.

There are many advantages in the use of solid-state lighting devices, such as light emitting diodes. First and foremost, the efficiency, intended as the electrical power effectively converted into light power, is far higher than conventional illumination systems. Second, the emission wavelength of each device can be tuned and the occupied area is on the microscopic scale, widening the number of potential applications and improving the portability of the final product.

Optoelectronic devices operating in the infrared region of electromagnetic spectrum have always been interesting due to their potential applications in telecommunications and thermal detection. The number of materials suited for the fabrication of photodetectors and light emitters is small. Up to now, narrow gap materials lilke HgCdTe, InGaAs, and InAsSb have been used for the fabrication of short and mid wave infrared optoelectronic devices.[88, 124] In spite of their performances, the fabrication costs remain high and technologies required to cool these devices down to the operating temperatures are expensive.

An interesting alternative to these materials are Ge and $Ge_{1-x}Sn_x$ alloy. Although Ge is usually employed in the fabrication of electronic devices, it was scarcely considered as a material for light emission or absorption due to its indirect energy gap and poor photodetection capabilities, compared to Si. However, the integrability of Ge with complementary metal-oxide semiconductor technology makes it an attractive cheaper alternative to other materials. Due to these reason, the research on potential optoelectronic applications of Ge never stopped and the first optically pumped laser have been fabricated.[128]

Potential applications of $Ge_{1-x}Sn_x$ alloy have been investigated first by Goodman[52] in 1983, and an intensive effort in the research activity lead to the developement of *ad-hoc* technological processes to incorporate *n* and *p* type dopant species into $Ge_{1-x}Sn_x$ lattice.[36, 55,

111, 130] As a result, many research groups have been able to fabricate and test simple $Ge_{1-x}Sn_x$ based photodetector devices.[46, 99, 127, 132]

In spite of the big experimental effort made to employ $Ge_{1-x}Sn_x$ as material for emission and absorption, no detailed investigation on the competition between intrinsic radiative and non-radiative recombination mechanisms has been performed up to now. The radiative and Auger recombination mechanisms are intrinsic properties of the material, depending on the electronic band structure, and cannot be improved by the fabrication process. Nonetheless, detailed investigations on Auger processes on Ge has been performed through second order perturbation theory models applied to simple analytical band structure models.[56, 57, 61, 62, 74] Furthermore, an analysis on the competition between radiative and Auger processes in $Ge_{1-x}Sn_x$ is still missing. Therefore, a detailed investigation on Auger recombination properties of strained and relaxed bulk Ge and on radiative and Auger recombination properties of bulk $Ge_{1-x}Sn_x$ is the subject of the first part of this work.

The first part of this work is devoted to the numerical determination of Auger recombination properties of relaxed and strained bulk Ge and Auger and radiative recombination lifetimes in relaxed bulk $Ge_{1-x}Sn_x$ at two different molar fractions. The recombination rates have been numerically computed through the application of a Green's function based model to the full electronic band structure of bulk material, computed through an empirical pseudopotential method.

In the last decade, A great deal of effort has been directed toward an optimal design of $In_xGa_{1-x}N$/GaN based light emitting diodes. One of the big advantages of $In_xGa_{1-x}N$/GaN based light emitting diodes relies in the tunable band gap energy, depending on indium molar fraction, allowing to fabricate devices that emit light potentially at any wavelength of the visible spectrum. However, the fabrication of GaN based light emitting diodes became possible only after 1989, when Isamu Akasaki, Hiroshi Amano, and Shuji Nakamura proposed a solution to the problem of incorporating and activating Mg atoms in GaN lattice[2, 85]. An achievement worth of the nobel prize in physics, obtained later in 2014.

The relevance and versatility of $In_xGa_{1-x}N$/GaN based light emitting diodes lead to further experiments and investigations uncovering a number of peculiar issues of these devices.[6][17] An important and controversial issue has been the so called *efficiency droop*. The signature of this phenomena is a reduction of emitted optical power as the injected current density increases over a threshold value. At the operating point, the device efficiency is sensibly quenched and the phenomena has been the subject of an intense research activity in past years. [19, 23, 27, 28, 63, 100, 115]

Recently, many research groups uncovered another problem undermining $In_xGa_{1-x}N$/GaN based light emitting diodes efficiency. The device optical power is known to decrease with temperature following an exponential law. However, over a threshold temperature the optical power is quenched down to fractions of its original value. This phenomena is called *thermal droop* and represents a potential issue due to the junction temperatures that GaN based light emitting diodes shows at the operating point.[16, 43, 60, 69, 83] The study of this phenomena from the perspective of device level numerical simulation is the subject of the second part of this work.

In the second part of this work, the *thermal droop* phenomena in $In_xGa_{1-x}N$/GaN based light emitting diodes is investigated from a device level modeling perspective. Among all the possible physiscs based mechanisms that could provide an explanation to this phenomena, the current contributions induced by Shockley-Read-Hall recombination processes, at different temperatures and injectetd current densities, are investigated and conclusions on their impact on this phenomena are drawn.

Contents

List of Figures

List of Tables

Part I

Numerical determination of optical recombination properties of Ge and $Ge_{1-x}Sn_x$

Introduction

In the field of infrared (IR) photodetectors, the goal is to find materials suitable for detection that works at operating temperature as close as possible to room temperature and to mitigate fabrication costs. A considerable number of narrow gap semiconductors (mainly III-V ternary alloys) are currently available for IR photodetectors fabrication: lattice matched indium arsenide antimonide on gallium antimonide, lattice matched indium gallium arsenide on indium phosphide, and mercury cadmium telluride on cadmium telluride. A cheaper and technologically ready alternative to those materials would be germanium and germanium-tin alloy.

Germanium posses an energy gap suitable for IR applications and has a high compatibility with integrated complementary metal-oxide semiconductor (CMOS) technology, representing a cheaper alternative to materials currently used for IR photodetector fabrication. Germanium has never been considered a suitable material for optoelectronic applications due to its indirect energy gap. Nevertheless, a lot of effort has been spent in understand how the optical properties of germanium changes under the effect of strain and doping.[30, 102, 116] It has been proven that the application of a minimum biaxial tensile strain around 2% allows to turn germanium into a direct energy gap material.[125] However, it is very hard to grow pseudomorphically strained germanium layers with the minimum level of biaxial strain required. Thus, a lot of effort has been devoted to the fabrication and characterization of Ge based nanostructures for which high strain levels can be achieved: uniaxially strained microbridges,[104] uniaxially strained nanowires,[105] and biaxially strained nanomembranes.[31] The Auger recombination properties represent an intrinsic characteristic of a material, and a limiting factor to the internal quantum efficiency of optoelectronic devices. Therefore, a deeper understanding of Auger processes in relaxed and strained Ge is required for an effective design of Ge based light emitters.

Other than germanium, a lot of interest has been focused on the germanium-tin ($Ge_{1-x}Sn_x$) alloy. This alloy offers a tunable energy gap, controlled by the molar fraction of α-tin, with an emission wavelength in the IR.[127] The fabrication of high quality and high purity $Ge_{1-x}Sn_x$ films has always been a challenging task. Due to the 1% equilibrium solubility of tin in germanium[47] and to the instability of α-Sn, which rapidly degrades to β-Sn at ambient temperature, only non-equilibrium techniques allowed to grow a stable alloy. However,

phase purity and compositional homogeneity prevented the formation of a stable alloy above 20% molar fraction.[58]

Signature of disorder effects, misfit dislocation, and phase separation are often detected in $Ge_{1-x}Sn_x$ samples[14, 15, 58] through transmission electron microscope (TEM) analysis and optical absorption coefficient measures. Furthermore, Urbach tail features, addressing compositional disorder, has always been detected in the measured optical absorption coefficient of $Ge_{1-x}Sn_x$ samples.

An enormous advantage is the full integration of $Ge_{1-x}Sn_x$ with Si-based technology. Novel deposition techniques allowed to grow pseudomorphic $Ge_{1-x}Sn_x$ on $Ge(001)$[110] and relaxed $Ge_{1-x}Sn_x$ on $Si(001)$[128]. Furthermore, the fabrication of a $Ge_{1-x}Sn_x$ based optically pumped laser by Wirths *et al.*[128] fostered the interest toward the use of this alloy as base material for IR emitters.

Detailed investigations on the incorporation of *n* and *p* dopant species into $Ge_{1-x}Sn_x$ lattice have been performed, novel deposition techniques have been developed,[36, 55, 111, 130] and number of research groups already fabricated and tested the photoresponse of simple $Ge_{1-x}Sn_x$ based devices.[46, 99, 132] Thus, the potential applications of these materials in IR integrated optoelectronic require a detailed investigation of their radiative and Auger recombination properties along with the absorption coefficient. An accurate numerical modelization is fundamental to assess material performances and the device efficiency under operating conditions.

Preliminary theoretical models[61, 62, 67, 68] describing Auger processes have been developed for theoretical analysis in ages when computational capabilities were extremely limited. Therefore, their predictive capabilities were bounded by the approximations required to obtain a close form expression for the equations involved.

Preliminary theoretical investigations on Auger recombinations have been conducted by Beattie and Landsberg, and later by Landsberg and Adams.[67, 68]They developed an approach, based on second order perturbation theory, to determine the Auger lifetime of electron and holes in semiconductors. Successively, Huldt extended the theory[67, 68] to the case of holes in germanium. He modeled the valence bands in the effective mass approximation and gave a quantitative estimate of direct[61] and phonon-assisted[62] (indirect) recombination rates. Later numerical investigations on Auger coefficients have been performed by Bertazzi *et al.*[19–21, 23, 26] and focused on the numerical determination of Auger lifetimes in HgCdTe and Auger coefficients in bulk InGaN and in InGaN/GaN quantum wells. A detailed comparison between Auger and radiative recombination lifetimes were performed by Wen *et al.*[126] in order assess performances of HgCdTe, InAsSb and InGaAs for IR photodetection applications.

Due to the novelty of $Ge_{1-x}Sn_x$, no prior works on its optical and Auger recombination properties are currently available in literature,

to the author's knowledge. However, also Ge didn't receive much attention in the past. While the optical recombination properties of Ge have been extensively studied, especially the absorption coefficient, the Auger recombination properties were not. An experimental attempt on measuring the Auger recombination coefficients in bulk Ge have been made by Auston *et al.*[5], while Huldt studied the problem from an analytic point of view in [61, 62]. No numerical studies of Auger recombinations in relaxed and strained Ge have been performed so far, to the Author's knowledge.

The current part presents a numerical determination of Auger recombination coefficient, radiative recombination coefficient, and absorption coefficient for relaxed and strained bulk germanium and for relaxed bulk germanium-tin alloy. The full electronic band structure of bulk materials is determined through an empirical pseudopotential method (EPM) code. Hereafter, the absorption and recombination coefficients are calculated through a Green's function based model applied to the computed electronic band structure.

The current part of this document is composed by four chapters. After this introductory chapter, three more chapters follow. Chap.2 reports on the physics based models and the numerical methods, Chap.3 reports the results obtained, and Chap.4 draws the conclusions.

Physics based model and numerical methods

2.1 THE ELECTRONIC BAND STRUCTURE

The electronic band structure of considered materials has been calculated by means of an Empirical Pseudopotential Method (EPM) code,[40, 41] that has already been used to compute the electronic band structure of bulk materials.[19, 51, 125, 126] The EPM theory is developed under the Hartree (or mean field) approximation, which assumes that each electron moves into an average field created by all other electrons, and the Born-Oppenheimer approximation, which assumes that the motion of atomic cores and the electron can be decoupled. Let's consider the time independent Schrödinger equation

$$\left[-\frac{\hbar^2}{2m_0} \nabla^2 + V(\mathbf{r}) \right] \Psi(\mathbf{r}) = E\Psi(\mathbf{r}), \tag{1}$$

in which $V(\mathbf{r})$ represents the potential accounting for electron-core and electron-electron interactions, $\Psi(\mathbf{r})$ represent the eigenvectors, and E the eigenvalues. Under the assumption of a perfect periodic lattice, the eigenfunctions of Schrödinger equation can be recast in the form of Bloch waves

$$\Psi(\mathbf{r}) = u_\mathbf{k}(\mathbf{r}) e^{i\mathbf{k}\cdot\mathbf{r}}, \tag{2}$$

in which $u_\mathbf{k}(\mathbf{r})$ represents the lattice periodic part and $e^{i\mathbf{k}\cdot\mathbf{r}}$ the slowly oscillating term. Subsequently, the lattice periodic part is expanded into plane waves as

$$u_\mathbf{k}(\mathbf{r}) = \sum_{n=1}^{N} B_n e^{i\mathbf{G}_n\cdot\mathbf{r}}, \tag{3}$$

in which B_n represent the expansion coefficients, $\mathbf{G}_n$ represent the plane wave vectors, and N represents the total number of plane waves in the expansion. The total number of plane waves (N) in the expansion will be determined by a cutoff energy. The expansion of the potential energy term ($V(\mathbf{r})$) in Fourier series is conveniently carried out over the set of plane waves that has already been exploited

$$V(\mathbf{r}) = \sum_{m=1}^{N} V(\mathbf{G}_m) e^{i\mathbf{G}_m\cdot\mathbf{r}}, \tag{4}$$

in which $V(\mathbf{G}_m)$ refers to the pseudopotential components expressed in the plane wave basis. The resulting equation represents the basis of EPM approach[41]

$$\frac{\hbar^2}{2m_0}|\mathbf{k}+\mathbf{G}_i|^2 B_i + \sum_j V\left(\mathbf{G}_{i-j}\right) B_j = E\left(\mathbf{k}\right) B_i. \tag{5}$$

The eigenvalues and eigenvectors represents the energy states and the coefficients B_n of the plane basis expansion, respectively. Furthermore, It has to be solved for each $\mathbf{k}$ point of interest in the reciprocal lattice.

The spin-orbit interaction term is taken into account. The related matrix element is given as[29, 118, 121, 125]

$$\langle \mathbf{k}_{i\nu}|\hat{H}_{SO}|\mathbf{k}_{j\eta}\rangle = \boldsymbol{\sigma}_{\nu\eta} \cdot \left(\mathbf{k}_i \times \mathbf{k}_j\right) \tag{6}$$
$$\times \left[\lambda^A \sin\left(\mathbf{G}_i - \mathbf{G}_j\right) \cdot \boldsymbol{\tau} - i\lambda^S \sin\left(\mathbf{G}_i - \mathbf{G}_j\right) \cdot \boldsymbol{\tau}\right],$$

where $\mathbf{G}_i$ and $\mathbf{G}_j$ are the reciprocal lattice vectors, $\boldsymbol{\sigma}_{\nu\eta}$ is the Pauli matrix, $\mathbf{k}_{i,j} = \mathbf{G}_{i,j} + \mathbf{k}$, and $\boldsymbol{\tau}$ is the atomic position vector. The symmetric and antisymmetric spin parameters are equal to

$$\lambda^S = \frac{\lambda_1 + \lambda_2}{2}, \tag{7}$$

$$\lambda^A = \frac{\lambda_1 - \lambda_2}{2}, \tag{8}$$

in which λ_1 and λ_2 are defined as

$$\lambda_1 = \mu\mathbf{B}_{nl}^{(1)}\left(k_i\right)\mathbf{B}_{nl}^{(1)}\left(k_j\right), \tag{9}$$

$$\lambda_2 = \gamma\mu\mathbf{B}_{nl}^{(2)}\left(k_i\right)\mathbf{B}_{nl}^{(2)}\left(k_j\right). \tag{10}$$

In Eq.9-10, the parameter γ is the ratio of spin-orbit energy of the free cation and anion atoms[59], and μ is an adjustable parameter to obtain the correct spin orbit energy for the material. The term $\mathbf{B}_{nl}^{(i)}(k)$ refers to the *i*-th atomic specie (with $i = \{1,2\}$) and is evaluated according to

$$\mathbf{B}_{nl}^{(i)}(k) = C\int_0^\infty \mathbf{j}_l(kr)\mathbf{R}_{nl}^{(i)}(r)r^2 dr, \tag{11}$$

where $\mathbf{j}_l(kr)$ is the spherical Bessel function of order *l*, $\mathbf{R}_{nl}^{(i)}(r)$ is the atomic wavefunction corresponding to the quantum numbers *n* and *l*, and C is a constant chosen to satisfy the identity[118, 125]

$$\lim_{k\to 0}\frac{\mathbf{B}_{nl}^{(i)}(k)}{k} = 1. \tag{12}$$

The evaluation of Eq.12 is facilitated through a proper choice of $\mathbf{R}_{nl}^{(i)}(r)$. In the present work, $\mathbf{R}_{nl}^{(i)}(r)$ is expanded through a set of basis functions obtained with the Roothaan-Hartree-Fock method[39]. The contribution of spin-orbit interactions is included as an additional potential term in $V(\mathbf{G}_{i-j})$ of Eq.5.

The atomic and spin potential used in the present work, for bulk zinc blende materials, are local and account for screening effects. These are function of wavevector q with functional dependence described by a spline interpolation, as reported in Fig.1.
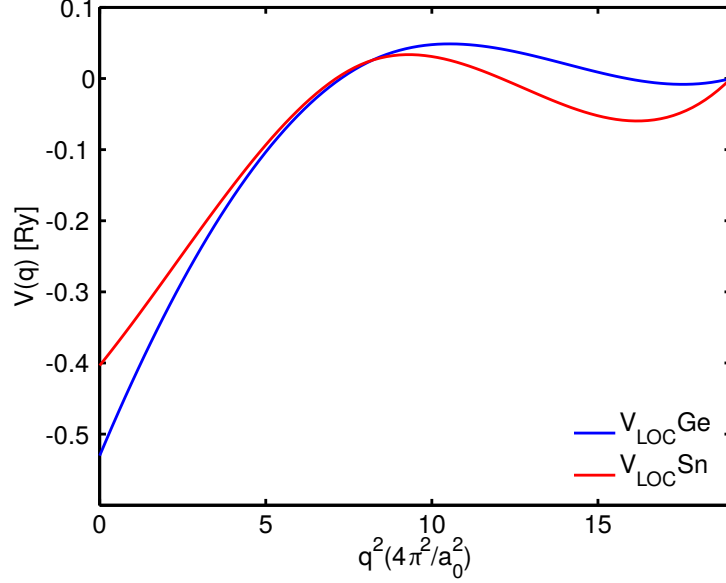
Figure 1: Spline interpolation of q-dependent local screened pseudopotentials for Ge and Sn.

In presence of a binary alloy, the EPM approach requires a further assumption in order to be applicable: the spatial distribution of the atomic species composing the alloy must be uniform in space, in order to fulfill the initial assumption of a perfect periodic lattice. Under this assumption, the atomic ans spin potential of the alloy are calculated as a linear interpolation, function of molar fraction, of the parameters of base atomic species

$$P_i^{(1_{1-x}2_x)} = xP_i^{(2)} + (1-x)P_i^{(1)}, \tag{13}$$

where $P_i^{(1,2)}$ is the i-th component of atomic or spin potential of base material (1 or 2) and $P_i^{(1_{1-x}2_x)}$ is the i-th component of atomic or spin potential of the alloy. In order to reproduce the electronic band structure of materials characterized by low structural disorder, such as $Ge_{1-x}Sn_x$,[84] a quadratic term is added to Eq.13

$$P_i^{(1_{1-x}2_x)} = P_i^{(1_{1-x}2_x)} - d_{(D,SO)}[x(1-x)]\left(P_i^{(1)} - P_i^{(2)}\right), \tag{14}$$

where d_D is the disorder parameter, and d_{SO} is the spin disorder parameter. The disorder and spin disorder parameter are tunable parameter used to reproduce experimental data on the electronic structure. The disorder parameters have been first introduced to study compositional disorder in the virtual crystal approximation in binary

Parameter	Unit	Ge	Sn
V_0	Ry	−0.5303	−0.4034
V_3	Ry	−0.2425	−0.2141
V_8	Ry	0.0210	0.0222
V_{11}	Ry	0.0479	0.0193
V_{19}	Ry	0.0	0.0000
γ	-	1.0	1.0
μ	-	0.00142	0.07132

Table 1: Non-local screened atomic potential and spin parameters for Ge and α-Sn.

and ternary alloys.[70] The non-periodic potential arising from compositional disorder is averaged out to a periodic effective disorder potential and this term is usually treated as a tunable parameter.[89]

The pseudopotential parameters adopted in this work have been reported in Tab.1. They represent the non-local screened atomic potentials, spin parameters (as reported in Eq.9-10) for germanium[125] and α-Sn. These parameters have been calculated starting from Ab-Initio results.

In contrast with DFT techniques, the EPM offers a reduced computational cost. In the calculation of the electronic band structure, the elementary lattice cell, composed by atoms at fixed positions, is assumed periodic along each direction of space. Therefore, in the virtual crystal approximation no optimization of atom position is required.

The calculated energy states are affected by the chosen pseudopotentials and by the cut-off energy chosen for the plane wave basis expansion. The cut-off energy determines the computational effort and the accuracy of the calculated energy bands. In general, the cut-off energy is set to reproduce DFT results on the energy bands up to a certain band index.

2.2   THE ABSORPTION AND RECOMBINATION MODELS

The absorption coefficient and the radiative recombination rate are critical quantities for an efficient design of passive and active optoelectronic devices. The model adopted for the physics based description of the absorption coefficient and radiative recombination rate is based on the Green's function formalism. The theoretical basis for this model can be found in literature books on many-body physics[64, 77], whereas the full derivation has been presented by Wen *et al.*[125] The model has been applied to study the optical emission and absorption properties of a number of bulk materials: Ge,[44] InGaAs, InAsSb and HgCdTe[123, 125, 126].

The phonon-assisted radiative recombination rate is give as[125]

$$R_{12}(\hbar\omega) = \frac{2n_r\omega}{\pi\hbar c_0^3 v\varepsilon_0} \int dE_1 \int dE_2 \sum_{\mathbf{k}} |P_{1,2}(\mathbf{k})|^2 \Theta(E_2)[1-\Theta(E_1)]$$
$$\times \delta(\mu_c - \mu_v + E_2 - E_1 - \hbar\omega) \text{Im}G_{l_1}^R(\mathbf{k}, E_1) \text{Im}G_{l_2}^R(\mathbf{k}, E_2),$$
(15)

while the net phonon-assisted absorption coefficient is given as[125]

$$\alpha_{12}(\hbar\omega) = \frac{2\pi}{nc_0 v\omega\varepsilon_0} \int dE_1 \int dE_2 \sum_{\mathbf{k}} |P_{1,2}(\mathbf{k})|^2 [\Theta(E_1)-\Theta(E_2)]$$
$$\times \delta(\mu_c - \mu_v + E_2 - E_1 - \hbar\omega) \text{Im}G_{l_1}^R(\mathbf{k}, E_1) \text{Im}G_{l_2}^R(\mathbf{k}, E_2).$$
(16)

In Eq.15-16 $\hbar\omega$ is the photon energy, subscripts 1 and 2 are the band indexes, n is the refractive index, c_0 is the speed of light in vacuum, ε_0 is the vacuum permittivity, $\Theta(E_i)$ is the energy dependent Heaviside function, $\text{Im}G_{l_1}^R(\mathbf{k}, E_1)$ is the imaginary part of the system retarded Green's function, $P_{1,2}(\mathbf{k})$ is the overlap integral between the eigenfunctions of state 1 and 2, and μ_c and μ_v are the quasi-Fermi levels for electron and holes, respectively.

The Auger recombination mechanism involve recombination processes of higher order with respect radiative processes. However, these are non-radiative processes and the competition between radiative an non-radiative processes is known as one of the causes for efficiency losses in devices for light emission/absorption under operating conditions.[19, 20, 23, 115] The novelty of a Green's function based approach to tackle the physics of Auger mechanisms has been introduced by Takeshima[107, 108] and Bardyszewsky and Yevick[12]. The Auger recombination rate is given as[44, 45, 125, 126]

$$R_{AR} = \frac{2\pi}{\hbar} \frac{V^3}{(2\pi)^9} \left[1 - e^{(\mu_v-\mu_c)/k_B T}\right]$$
$$\times \int d\mathbf{k}_1 d\mathbf{k}_2 d\mathbf{k}_{1'} d\mathbf{k}_{2'} |M_{ee}|^2 \delta(\mathbf{k}_1 + \mathbf{k}_2 - \mathbf{k}_{1'} - \mathbf{k}_{2'})$$
$$\times \int dE_1 dE_2 dE_{1'} dE_{2'} \Theta(E_1)\Theta(E_2)[1-\Theta(E_{1'})][1-\Theta(E_{2'})]$$
$$\times \text{Im}G_{l_1}^R(\mathbf{k}_1, E_1) \text{Im}G_{l_2}^R(\mathbf{k}_2, E_2) \text{Im}G_{l_{1'}}^R(\mathbf{k}_{1'}, E_{1'}) \text{Im}G_{l_{2'}}^R(\mathbf{k}_{2'}, E_{2'}).$$
(17)

In Eq.17 $|M_{ee}|^2$ is the overlap integral between the eigenfunctions involved in the transition and V is the volume of the elementary lattice cell. The model reported in Eq.17 overcome the numerical singularities of second order perturbation theory when the virtual state overlaps to the real state. Nonetheless, the numerical accuracy of second order perturbation theory based models has been long criticized due to their numerical singularities.[32, 109]

The evaluation of broadening term, namely the imaginary part of the system retarded Green's function ($\mathrm{Im}G^R_{l_i}(\mathbf{k}, E_i)$), reported in Eq.15-17 represent the core of the Green's function based model. The broadening term is given as[44, 125, 126]

$$\mathrm{Im}G^R_{l_i}(\mathbf{k}, E) = -\frac{1}{\pi} \frac{\mathrm{Im}\Sigma_i(\mathbf{k}, E)}{[E - E_i - \mathrm{Re}\Sigma_i(\mathbf{k}, E)]^2 + [\mathrm{Im}\Sigma_i(\mathbf{k}, E)]^2}, \quad (18)$$

where E_i is the i-th energy state, $\mathrm{Im}\Sigma_i(\mathbf{k}, E)$ and $\mathrm{Re}\Sigma_i(\mathbf{k}, E)$ are the imaginary and real part of self-energy, respectively. The effect of perturbations (i.e. electron-phonon interactions) is expressed by expanding the system self-energy in terms of Dyson's equation.[77] To the description of radiative and Auger recombinations, it is sufficient to retain only the lowest order in the expansion. Therefore, we express the imaginary part of self-energy as[126]

$$\mathrm{Im}\Sigma_i(\mathbf{k}, E) = -\pi \sum_\nu \int \frac{d\mathbf{k}'}{(2\pi)^3} \left| g_\nu(\mathbf{k}' - \mathbf{k}) \right|^2 B_{ii}(\mathbf{k}, \mathbf{k}')$$
$$\times \left\{ [1 + P(\hbar\omega_\nu) - \Theta(E - \hbar\omega_\nu)] \delta(E - \hbar\omega_\nu - E_i(\mathbf{k}')) \right.$$
$$\left. + [P(\hbar\omega_\nu) + \Theta(E + \hbar\omega_\nu)] \delta(E + \hbar\omega_\nu - E_i(\mathbf{k}')) \right\}, \quad (19)$$

where $B_{ii}(\mathbf{k}, \mathbf{k}')$ is the overlap between the electron eigenfunctions with wavevectors $\mathbf{k}$ and $\mathbf{k}'$, $P(\hbar\omega_\nu)$ is the Bose-Einstein distribution, $\Theta(E \pm \hbar\omega_\nu)$ is the step function, and $g_\nu(\mathbf{k}' - \mathbf{k})$ is the matrix element for the ν-th carrier-phonon interaction mechanism. For the study of Ge and GeSn, we considered acoustic and non-polar optical carrier-phonon interaction mechanisms, characterized by the following matrix elements

$$|g_{AC}(q)|^2 = \frac{\Xi_d^2 \hbar \omega_{ac}(q)}{2c_l} \frac{q^4}{(q^2 + \lambda^2)^2}, \quad (20)$$

$$|g_{NPO}(q)|^2 = \frac{\hbar D^2 v_s^2}{2\bar{c}\omega_{op}(q)} \frac{q^4}{(q^2 + \lambda^2)^2}. \quad (21)$$

In Eq.20,21, $q = \left| \mathbf{k}' - \mathbf{k} \right|$ is the phonon wavevector, c_l and c_t are the longitudinal and transverse elastic constants, $\bar{c} = c_l/3 + 2c_t/3$ is the average lattice constant, and v_s is the sound velocity.

The dielectric function model is of great importance, especially in case of Auger transitions where the Coulomb interaction between carriers with different wavevectors mediates the process. Therefore, the code implements a static wavevector dependent screened dielectric function model given by

$$\varepsilon(\mathbf{q}) = \frac{c_1}{|\mathbf{q}|^{c_2} + c_3}, \quad (22)$$

where c_1, c_2, and c_3 are obtained by fitting results from the random phase approximation.[117]

Parameter	Unit	Ge	$Ge_{0.91}Sn_{0.09}$	$Ge_{0.82}Sn_{0.18}$
c_l	GPa	128.5	117.950	114.100
c_t	GPa	64.4	64.769	65.522
ε_0	-	16.6	16.880	17.440
ε_∞	-	16.6	16.880	17.440
$\hbar\omega_{op}$	meV	37.05	35.930	35.060
Ξ_d	eV	9.1	9.1	9.1
$D\,(L_{6c})$	10^8 eV/cm	12.17	12.17	12.17
$D\,(L_v)$	10^8 eV/cm	10.0	10.0	10.0

Table 2: Alloy parameters for $Ge_{1-x}Sn_x$ in E-SWIR and MWIR configurations. [49, 86] The alloy parameters result from a linear interpolation of Ge and Sn values.

The total Auger recombination rate can be calculated starting from the relation $R_{AR} = (nC_n + pC_p)(np - n_i^2)$, where n and p are the excess electron and hole concentrations, n_i is the intrinsic carrier concentration, and C_n and C_p are the Auger coefficients for electron and hole, respectively. On the opposite hand, given the Auger recombination rate for two type of transitions, electron-electron-hole (R_{AR}^{eeh}) and hole-hole-electron (R_{AR}^{hhe}), the Auger coefficients are given by

$$C_n = \frac{R_{AR}^{eeh}}{n\left(np - n_i^2\right)}, \qquad C_p = \frac{R_{AR}^{hhe}}{p\left(np - n_i^2\right)}. \tag{23}$$

The Auger lifetimes can be written in terms of Auger coefficients as

$$\tau_{eeh} = \frac{1}{n^2 C_n}, \qquad \tau_{hhe} = \frac{1}{p^2 C_p}. \tag{24}$$

In this work, the Auger lifetimes and coefficients are calculated always for the minority carrier population: holes for *n*-doped material and electron for *p*-doped material. In case of an intrinsic material, coefficients and lifetimes have been calculated for both electron and holes.

For radiative recombination, equations similar to Eq.23-24 holds for radiative recombination coefficients and lifetimes, respectively. These are given by

$$B = \frac{R_{RR}}{np - n_i^2}, \qquad \tau_{RAD} = \frac{1}{\{n|p\}\,B}, \tag{25}$$

where $\{n|p\}$ stands for the carrier concentration type of minority carriers: n or p.

The band structure calculated through the EPM technique represent the 0 Kelvin band structure. The effect of a finite temperature has been included and implemented as rigid shift of all conduction states.

The temperature induced shift of the energy gap has been included for both materials, Ge and GeSn. In case of Ge, this work follows the experimental data on the temperature induced shift of the energy gap given by Madelung.[86] In case of GeSn, a uniform consensus on the temperature induced shift of the energy gap has not been reached yet. However, Freitas *et al.*[50] reported that a temperature induced shift of the energy gap equal to the one used for Ge represents a good approximation. Therefore, in this work the same approximation has been adopted.[50]

In the calculation of the recombination properties of $Ge_{1-x}Sn_x$, the effect of a uniform doping concentration has been included. For a given doping type and concentration, an equilibrium concentration of electron and hole can be retrieved through law of mass action. Given the equilibrium free carrier concentrations, and assuming the semiconductor in quasi-equilibrium conditions, any deviation from the equilibrium values (n_0 and p_0) can be described by

$$n_0 + \delta n = \int_0^{+\infty} \frac{g_{DOS}(E - E_c)}{1 + e^{E - E_c - \mu_c} K_b T} dE, \tag{26}$$

$$p_0 + \delta p = \int_{-\infty}^{0} \frac{g_{DOS}(E - E_v)}{1 + e^{\mu_v - E + E_v} K_b T} dE. \tag{27}$$

In equations 26 and 27, $g_{DOS}(E)$ correspond to the density of states, μ_c and μ_v to the quasi-Fermi levels, δn and δp to the excess carrier concentrations, and E_c and E_v to the conduction and valence band edges. Therefore, given the doping type and concentration, and the excess carrier concentrations, equations 26 and 27 can be numerically inverted to obtain the quasi-Fermi levels.

The calculated quasi-Fermi levels are plugged in Eq.15-17 in order to calculate the optical recombination properties of the material for any given doping configuration and excess carrier concentration.

Numerical simulations and results

3.1 NUMERICAL SIMULATION METHOD

The first step of the simulation is to perform the tetrahedralization of irreducible wedge in reciprocal lattice and the calculation of the electronic band structure of bulk material. The discretization procedure is part of the EPM code that has been used by Wen *et al.* in a number of works,[123, 125, 126] and further details can be found in[122].

The irreducible wedge is regarded as the minimal volume of the Brillouin zone that can reproduce any other wedge of the full Brillouin zone by a finite number of geometrical rotations, as reported in Fig.2. Under the action of a biaxial tensile strain on real lattice atoms, the geometry of the first Brillouin zone strains isotropically on the k_x-k_y plane. This deformation causes the loss of symmetry operations $k_z = k_x$ and $k_x = k_y$ therefore modifying the shape of the irreducible wedge, as reported in inset (b) of Fig.2. In the case of a relaxed material, any point in the irreducible wedge can be projected onto any other wedge through combinations of the following symmetry operations

$$\hat{T}_{xy} = \begin{pmatrix} 0 & 1 & 0 \\ 1 & 0 & 0 \\ 0 & 0 & 1 \end{pmatrix}, \quad \hat{T}_{xz} = \begin{pmatrix} 0 & 0 & 1 \\ 0 & 1 & 0 \\ 1 & 0 & 0 \end{pmatrix}, \quad \hat{T}_{yz} = \begin{pmatrix} 1 & 0 & 0 \\ 0 & 0 & 1 \\ 0 & 1 & 0 \end{pmatrix},$$

$$\hat{T}_{\{ijl\}} = \begin{pmatrix} i & 0 & 0 \\ 0 & j & 0 \\ 0 & 0 & l \end{pmatrix}, \quad \text{with } i = \pm 1, j = \pm 1, l = \pm 1. \tag{28}$$

In Eq.28, $\hat{T}_{ij}$ terms represent a symmetry operation of the type $k_i = k_j$, and $\hat{T}_{\{ijl\}}$ represent a symmetry operation of the type $(k_x, k_y, k_z) = (i \cdot k_x, j \cdot k_y, l \cdot k_z)$. Therefore, the total number of symmetry operations for a relaxed diamond cubic lattice is 48 (2 for each $\hat{T}_{ij}$ and 2^3 for all $\hat{T}_{\{ijl\}}$ terms) meaning that the irreducible wedge will be 1/48 of the volume of the total Brillouin zone. When a biaxial tensile strain is applied the symmetry operations $\hat{T}_{xz}$ and $\hat{T}_{yz}$ are lost accounting for an expansion of the irreducible wedge up to three times its original volume, as reported in inset (b) of Fig.2. Therefore, the irreducible wedge of a biaxially strained cubic diamond lattice occupies 1/16 of the volume of its first Brillouin zone.

The set of high symmetry points and paths for the diamond cubic reciprocal lattice is used to define the boundaries of the irreducible
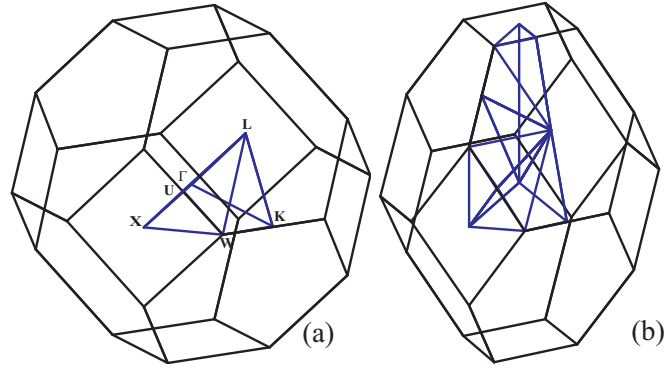
Figure 2: (a) First Brillouin zone (black) and irreducible wedge (blue) of diamond cubic reciprocal lattice. The greek letters L, Γ, U, X, W, and K identify the high symmetry points and the blue lines the high symmetry path. (b) A tensile biaxial strain is applied. The Brillouin zone strains and the irreducible wedge changes due to the lost symmetry on the vertical axis.
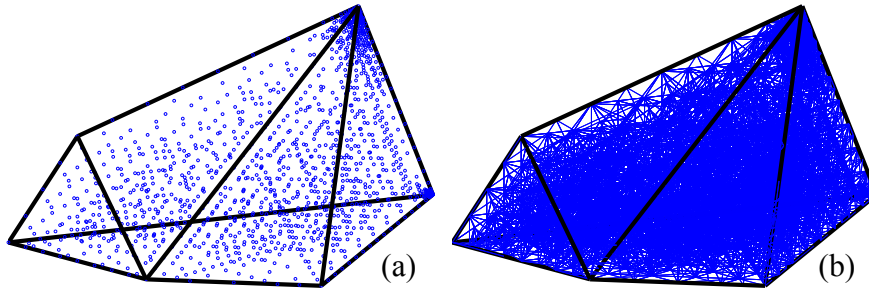
Figure 3: (a) Unstructured discretization of relaxed diamond cubic reciprocal lattice irreducible wedge featuring a total of 1639 points. The mesh resolution has been increased around the L point. (b) The corresponding tetrahedralization.

wedge. In order to reduce the error introduced by the numerical implementation and to keep a reasonable computational time, the irreducible wedge has been discretized through a band-adaptive non uniform meshing procedure. The discretization process takes place in two steps: a non-uniform discretization procedure over the whole irreducible wedge and a further refinement procedure around a single point. Starting from the $E(\mathbf{k})$ relations of the bands involved in the transition, the discretization procedure takes the energy value at the four vertices of a tetrahedron, performs a linear interpolation at the mid-point of each edge, and calculates the interpolation error with the true energy value. If all the calculated errors are smaller than a reference value, the tetrahedralization procedure ends. If one of the conditions on the error is not satisfied, the current tetrahedron is splitted in smaller tetrahedrons, considering the mid-point of each edge as a new vertex, and the procedure is reiterated over each generated tetrahedron. This procedure ensures a finer mesh in zones of the reciprocal lattice where the $E(\mathbf{k})$ is not linear. The second step of the

discretization process is to perform a further refinement around a specific point of reciprocal lattice. This is done to increase the mesh resolution in the neighbourhood of a specific point, in order to capture further details of the band structure. In case of Ge and $Ge_{1-x}Sn_x$, indirect transitions play an essential role and the refinement step is carried out around the L point, as reported in inset (a) of Fig.3.

The absorption and radiative recombination equations (Eq.15-16) are directly numerically solved. However, the numerical resolution of Eq.19 is not straightforward. The volume integral in self-energy equation (Eq.19) has been numerically evaluated through the tetrahedron method.[71] By exploiting the condition given by the delta-function, the volume integral turns into a surface integral of equi-energetic surfaces that are linearly interpolated through each tetrahedron. Despite the fact that higher order methods could be used, the use of an non-uniform tetrahedral mesh ensures an elevated accuracy of the method and an affordable computational cost.

The sixteen-fold integral appearing in Auger recombination rate equation (Eq.17) cannot be evaluated directly. After the simplification obtained through the integration of the delta function, the remaining thirteen-fold integral is solved through a Monte Carlo technique. Provided the selection of a random initial state, a rejection technique is applied to the selection of the final states. Once the randomized states satisfies the rejection condition, the integral value is updated with the current sample and then is recorded in the simulation history. The Monte-Carlo procedure stops when the ratio between the standard deviation and the average value of computed integral gets smaller than the 0.001, calculated over the latest thousand records in the simulation history.

The formulas presented in Eq.15-17 are valid for indirect transitions. In order to compute the recombination rate for direct transition, the limit of Eq.19 for $Im\Sigma(\mathbf{k}, E) \to 0$ and $Re\Sigma(\mathbf{k}, E) \to 0$ has to be taken. Therefore, in absence of any carrier-phonon interaction the limit yield a delta function, namely $\lim_{\Sigma(\mathbf{k},E)\to 0} ImG_{l_i}^R(\mathbf{k}, E) = -\delta(E - E_i)$. This operation allows to neglect any contribution coming from carrier-phonon interactions accounting for direct transitions only.

The calculation for the absorption coefficients and radiative recombination rate should be applied to direct and indirect transitions taking place between the first conduction band and each valence band. However, the contribution of transitions taking place between the first conduction band and the split-off band results to be negligible. Therefore, the calculations accounted for transitions taking place between first conduction band and heavy hole band and between first conduction band light hole band.

The number of possible transitions is higher in case of Auger recombinations. The valence and conduction bands have been numbered:

starting from the lowest valence band, labeled as 1, the top valence band is labeled 4 and the first conduction band is labeled 5. An Auger transition is identified by four numbers: the first two addressing the initial bands and the last two the final bands. The first transition, mediated by Coulomb interaction, is considered taking place between the first conduction state and the heavy hole band for both *eeh* and *hhe* processes (transition between bands 5 and 4). The initial and final states for the scattered carrier are chosen according to the type of process. For *eeh* processes, the initial state is always chosen to be the first conduction band, while the final state is chosen to be the first or second conduction bands (transition between 5 and 5 or 6). For *hhe* processes, the initial state is always chosen to be the heavy hole band, while the final state is chosen to be the heavy or light hole bands (transition between 4 and 4 or 3). Therefore, the total Auger recombination rate is evaluated as the sum of direct and indirect recombination rates for the following set of Auger transitions: 5545, 5546, 4454, and 4453.

The quasi-Fermi levels are required for Eq.15-16. The quasi-Fermi levels have been retrieved by numerical inversion of the following equations

$$n = \int_{E_c}^{+\infty} \frac{g\left(E\right)}{1 + e^{\frac{E - F_n}{K_b T}}} dE, \qquad n = \int_{-\infty}^{E_v} \frac{g\left(E\right)}{1 + e^{\frac{F_p - E}{K_b T}}} dE, \qquad (29)$$

given the injected free carrier concentrations n and p. In Eq.29 $g\left(E\right)$ is the density of states obtained from the full band structure calculation, $K_b T$ is the energy equivalent of temperature T, E_c and E_v are the conduction and valence band edges, and F_n and F_p are quasi-Fermi level for electron and hole, respectively.

3.2   SIMULATION RESULTS

Results presented in this section have been published in [45].

3.2.1   *Germanium*

The band structure calculation for germanium is reported in Fig.4. The two cases depicted in Fig.4 represent relaxed and strained germanium, with an applied biaxial tensile strain equal to 2.1%. Furthermore, the applied strain is enough to turn the material into a direct energy gap semiconductor.

The results for Auger recombination coefficients have been calculated and presented by the author in [44] for Ge at 300K under three strain configurations: relaxed, and biaxially strained at 1.4% and 2.1%. The material is assumed intrinsic and under injection conditions in which the free carrier concentration n and p in the material are set. The chosen injection conditions satisfies the equation $n = p$ and five values for the injected free carrier concentration have been chosen,
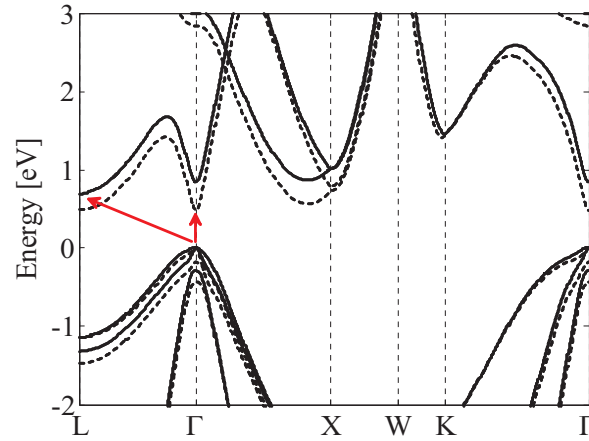
Figure 4: Germanium electronic band structure along the high symmetry paths.[44] The greek letters L, Γ, U, X, W, and K identify the high symmetry points. Two configurations are reported, relaxed (solid) and biaxially strained (dashed). Red arrows refer to the fundamental gap in both strain configurations.

namely 10^{16} cm^{-3}, 10^{17} cm^{-3}, 10^{18} cm^{-3}, 10^{19} cm^{-3}, and $5 \cdot 10^{19}$ cm^{-3}

In case of relaxed Ge, the dominant class of Auger processes is direct *hhe*. As depicted in Fig.5, the direct *hhe* processes show an Auger coefficient comprised between 10^{-32} cm^{6}s^{-1} and 10^{-31} cm^{6}s^{-1}, which is two order of magnitude higher than direct *hhe*. According to literature, indirect Auger processes should be dominant, as presented by Haugh[57], Lochmann[74], and Huldt[61, 62]. However, these early works adopted an analytic framework where approximations were due to tailor down the complexity of the problem and only the top conduction and valence bands were considered as initial and final states for the scattered particle.

In order to validate this results, a comparison with experimental results is due. An early work from Auston *et al.*[5] estimated a total Auger coefficient for relaxed Ge of $1.1 \cdot 10^{-31}$ cm^{6}s^{-1}, given a free carrier concentration equal to $3.4 \cdot 10^{20}$ cm^{-3}. However, the free carrier concentration reported in the experiment is fairly above the threshold at which many-body effects onsets ($\approx 10^{20}$ cm^{-3}), and the numerical model employed in this work is not tailored to include them. Therefore, results from this work cannot be compared with the values presented by Auston *et al.*. To the author's knowledge, no other literature references are available on the subject.

The dominant class of Auger process changes with an increasing level of biaxial tensile strain, as reported in Fig.5-7. When the a tensile biaxial strain is applied, the *eeh* processes assume a dominant role, especially direct *eeh* processes. The variation of total *eeh* and *hhe* Auger recombination coefficients function of the applied biaxial tensile strain is reported in Fig.8 for a fixed free carrier concentration
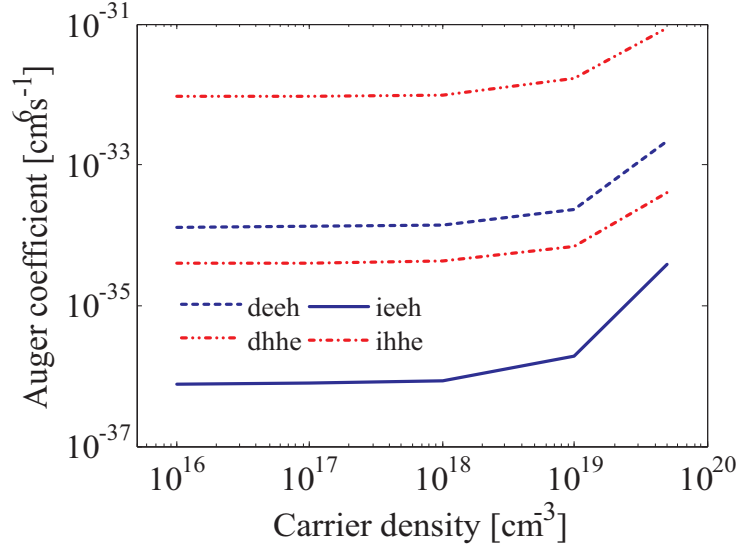
Figure 5: Auger coefficients for relaxed Ge for direct and indirect *eeh* transitions (deeh and ieeh), and direct and indirect *hhe* transitions (dhhe and ihhe). [44]

$n = p = 10^{19}$ cm^{-3}. It has been observed that *hhe* processes dominate up to a strain level of $\approx 0.35\%$, whereas *eeh* processes dominate at higher strain levels.

To the purpose of device-level modeling, an analytic formulation for C_n and C_p is given by

$$C_n = \frac{10^\gamma n^{\alpha \log_{10} n + \beta - 1}}{np - n_i^2}, \tag{30}$$

$$C_p = \frac{10^\gamma p^{\alpha \log_{10} p + \beta - 1}}{np - n_i^2}, \tag{31}$$

where α, β and γ are fitting parameters reported in Tab.3.

C_n	ϵ	α_0	β_0	γ_0	α_1	β_1	γ_1
	0%	0.0110	2.6402	-30.9373	0.6698	-21.5429	190.9124
	1.4%	-0.0311	4.0245	-38.2052	-0.0691	5.4993	-52.4502
	2.1%	-0.0040	3.1314	-30.8437	-0.0158	3.5507	-34.5862
C_p	ϵ	α_0	β_0	γ_0	α_1	β_1	γ_1
	0%	0.0114	2.6257	-28.9705	0.4574	-13.6881	120.1814
	1.4%	0.0056	2.8006	-28.9658	0.1432	-2.1336	15.2870
	2.1%	-0.0293	3.8723	-36.8335	0.2610	-6.5825	57.2865

Table 3: Fitting parameters for C_n (top) and C_p (bottom), at different biaxial tensile strain deformations. Subscript 0 refers to carrier densities $\leqslant 10^{18}$ cm^{-3}, while subscript 1 refers to carrier densities $\geqslant 10^{18}$ cm^{-3}. The content of this table has already been published in[44]
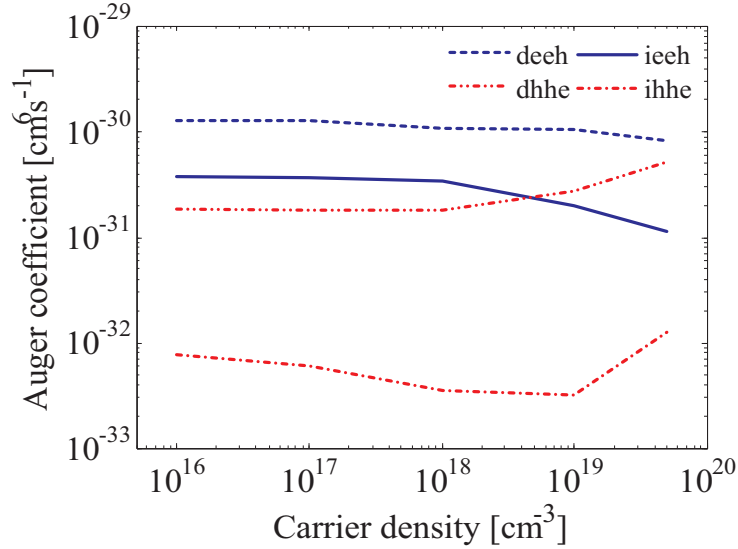
Figure 6: Auger coefficients for biaxially strained Ge (1.4%) for direct and indirect *eeh* transitions (deeh and ieeh), and direct and indirect *hhe* transitions (dhhe and ihhe). [44]

3.2.2 *Germanium-tin alloy*

The numerical determination of the electronic band structure of $Ge_{1-x}Sn_x$ alloy took place for Sn molar fractions comprised between 0% and 20%. The choice of this range has been constrained by the availability of experimental results on the energy gap and the work of Freitas *et al.*[50] has been taken as reference for the calculation of the band structure. The disorder and spin disorder parameters (d and d_{SO}) have been used as fitting parameters to reproduce results presented by Freitas *et al.*[50]. Their results have been reproduced with reasonable accuracy - as depicted in Fig.9 - by setting $d = -0.3$ and $d_{SO} = -10.0$. According to results reported in Fig.9, the crossover between the L and Γ minimum takes place $\approx 11\%$ for the EPM results.

The effective mass for valence and conduction bands have been extracted from band structure calculations. The effective mass along different high symmetry paths , namely Σ, Δ, and Λ, for the i-th band have been calculated and an overall effective mass has been calculated as

$$\frac{1}{m_i} = \frac{1}{m_i^{(\Sigma)}} + \frac{1}{m_i^{(\Delta)}} + \frac{1}{m_i^{(\Lambda)}}. \tag{32}$$

On the range of considered molar fractions, the effective mass for the first conduction, heavy hole, light hole, and split-off bands have been calculated and reported in Fig.10. While the effective mass for the first conduction band calculated at the L point remains constant, the effective masses for conduction, heavy hole, and light hole bands
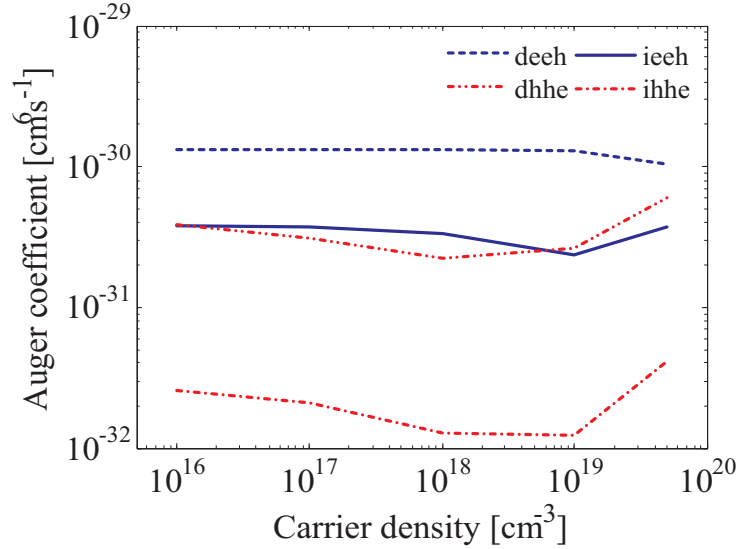
Figure 7: Auger coefficients for biaxially strained Ge (2.1%) for direct and indirect *eeh* transitions (deeh and ieeh), and direct and indirect *hhe* transitions (dhhe and ihhe). [44]

decrease with molar fraction. The only exception is the effective mass for split-off band, which registered an increment with molar fraction.

The interest is to study the recombination properties of $Ge_{1-x}Sn_x$ alloy in two configurations corresponding $\lambda = 2.7$ μm and $\lambda = 5$ μm cutoff wavelength. However, molar fraction and temperature represent two degrees of freedom that cannot be uniquely chosen to obtain the desired cutoff wavelengths, as reported in Fig.11. Therefore, the temperature has been fixed to 140 K for $\lambda = 5$ μm and 240 K for $\lambda = 2.7$ μm. Given the temperature, the molar fractions have been uniquely determined as 18% for $\lambda = 5$ μm and 9% for $\lambda = 2.7$ μm.

The electronic band structure for the two configurations have been reported in Fig.12. The $Ge_{0.91}Sn_{0.09}$ configuration show an indirect energy gap, while the $Ge_{0.82}Sn_{0.18}$ configuration show a direct energy gap. Nonetheless, the the energy gap measured at L point for $Ge_{0.91}Sn_{0.09}$ is only ≈ 10 meV smaller than the one measured at the Γ point.

The computed absorption coefficient for $Ge_{0.91}Sn_{0.09}$ and $Ge_{0.82}Sn_{0.18}$ is reported in Fig.13. A pronounced indirect absorption edge, at energies close to the energy gap, is observed for $Ge_{0.91}Sn_{0.09}$; a feature that can be attributed to the indirect nature of the energy gap. Instead, $Ge_{0.82}Sn_{0.18}$ show a sharp absorption edge due to the direct energy gap and no contribution from indirect transitions is observed.

The Auger and radiative recombination lifetime for $Ge_{0.91}Sn_{0.09}$ and $Ge_{0.82}Sn_{0.18}$ have been calculated considering a lightly *n*-type and *p*-type doped semiconductor. The doping concentrations (both *n*-type
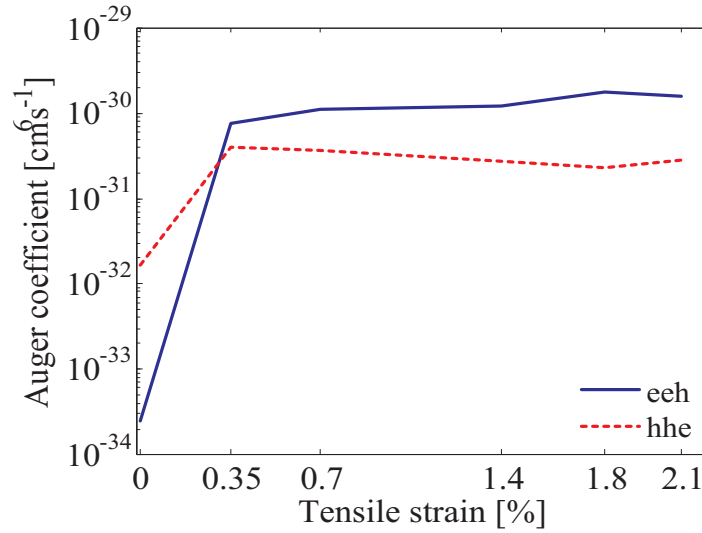
Figure 8: Total Auger coefficients for Ge under different strain conditions at fixed carrier density $n = p = 10^{19}$ cm^{-3}.[44]

and p-type) have been chosen to be 10^{15} cm^{-3} and 10^{17} cm^{-3} for both Ge$_{0.91}$Sn$_{0.09}$ and Ge$_{0.82}$Sn$_{0.18}$.

The competition between radiative and Auger lifetime in Ge$_{0.91}$Sn$_{0.09}$ at 240 K is reported in Fig.14 for a doping concentration of 10^{15} cm^{-3} and in Fig.15 for a doping concentration of 10^{17} cm^{-3}. It has to be observed that the radiative lifetime are almost independent from the doping type. A similar behaviour is observed in the Auger lifetimes for minority carriers.

The competition between radiative and Auger lifetime in Ge$_{0.82}$Sn$_{0.18}$ at 140 K is reported in Fig.16 for a doping concentration of 10^{15} cm^{-3} and in Fig.17 for a doping concentration of 10^{17} cm^{-3}. Also in this case, the radiative lifetime are independent from the doping type. Furthermore, the radiative lifetime saturate to 10^{-7} s at excess carrier concentrations higher that 10^{18} cm^{-3}. The minority carrier Auger lifetime for the n-doped semiconductor are six orders of magnitude smaller than the case of p-doped semiconductor. Therefore, the p-doped Ge$_{0.82}$Sn$_{0.18}$ offer theoretical performances suitable for practical applications.

A comparison between the radiative recombination coefficient of Ge$_{0.91}$Sn$_{0.09}$ and Ge$_{0.82}$Sn$_{0.18}$ is reported in Fig.18 for a doping concentration of 10^{15} cm^{-3} and in Fig.19 for a doping concentration of 10^{17} cm^{-3}. At the lower doping concentrations, both material configurations show a constant radiative recombination coefficient at all excess carrier concentrations. However, at the higher doping concentration, the Ge$_{0.82}$Sn$_{0.18}$ radiative recombination coefficient drops down of two orders of magnitude when the excess carrier concentration goes beyond 10^{17} cm^{-3}. In terms of performances, Ge$_{0.91}$Sn$_{0.09}$ offer overall better emission rates than Ge$_{0.82}$Sn$_{0.18}$.
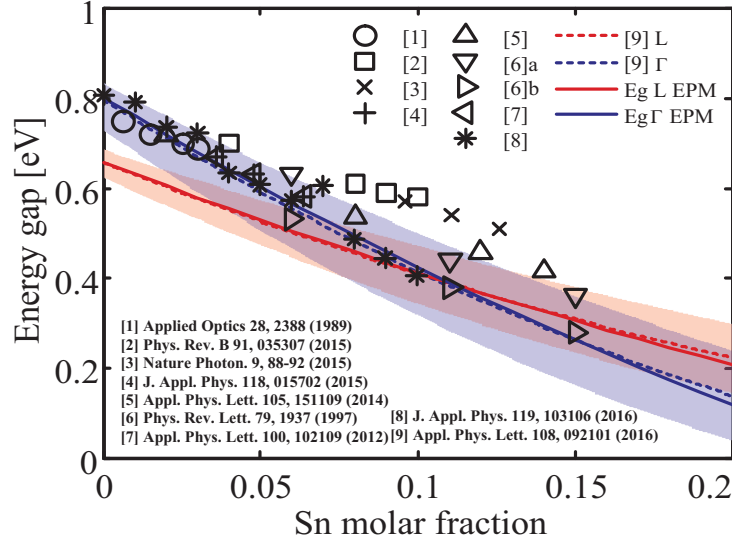
Figure 9: Experimental data available on $Ge_{1-x}Sn_x$ energy gap at 300 K. Shaded areas and dashed lines represent the standard deviation and average value, respectively, of cluster expansion method results from Freitas *et al.*[50]. Continuous lines represent the energy gap values calculated in this work.[45]

The Auger recombination coefficient for $Ge_{0.91}Sn_{0.09}$ doped *n*-type and *p*-type are constant, of the order of $\approx 10^{-30}$ cm^6 s^{-1}, as reported in Fig.20 and Fig.21. On the other hand, the doping type is discriminant for $Ge_{0.82}Sn_{0.18}$. The Auger coefficient for the *n*-doped $Ge_{0.82}Sn_{0.18}$ is six orders of magnitude higher than the *p*-doped $Ge_{0.82}Sn_{0.18}$. It is possible to say that Auger recombinations are suppressed in *p*-doped $Ge_{0.82}Sn_{0.18}$.

The deformation of the band structure due to changes in the molar fraction and temperature can be decoupled in two effects: a band gap shift and a deformation of the energy bands. The variation of the energy gap changes the activation energy of the Auger process, while the deformation of the energy bands impacts on the number of available final states for an Auger transition. An additional set of simulations, aimed to discern the contribution of these effects on the Auger rate, revealed that the discriminant feature is the deformation of the energy bands. On the other hand, the shift of the energy gap is not enough to explain the differences between $Ge_{0.91}Sn_{0.09}$ and $Ge_{0.82}Sn_{0.18}$ Auger recombination properties.
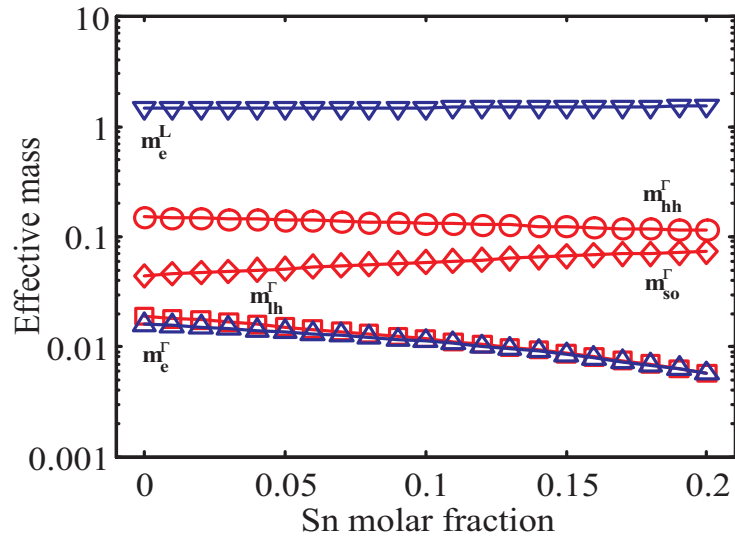
Figure 10: Effective mass computed at Γ and L high symmetry points of reciprocal lattice. The reported effective mass for electron (blue) and hole (red) is an average over different directions, calculated at the band minimum as reported in Eq.32. [45]
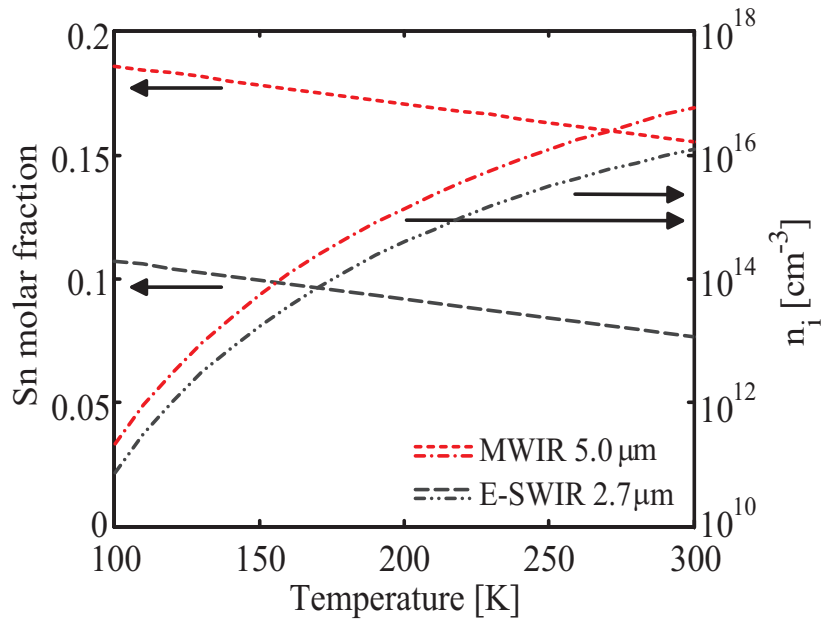
Figure 11: Intrinsic carrier concentration (right axis) and Sn molar fraction (left axis) corresponding to the chosen cutoff wavelengths (in legend) function of temperature. Black arrows refer each curve to the proper axis.[45]
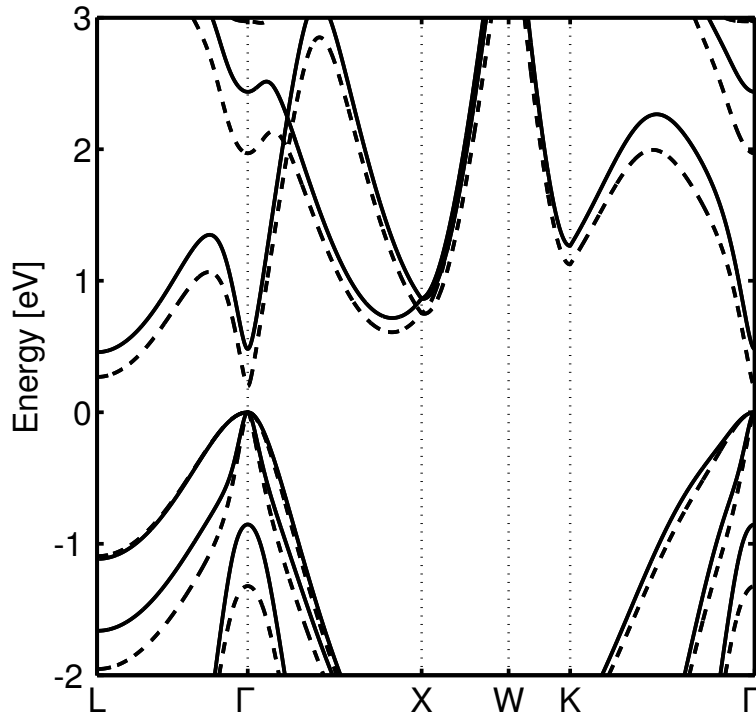
Figure 12: Germanium-tin band structure for two configuration $Ge_{0.91}Sn_{0.09}$ and $Ge_{0.82}Sn_{0.18}$ represented as solid and dashed lines, respectively.
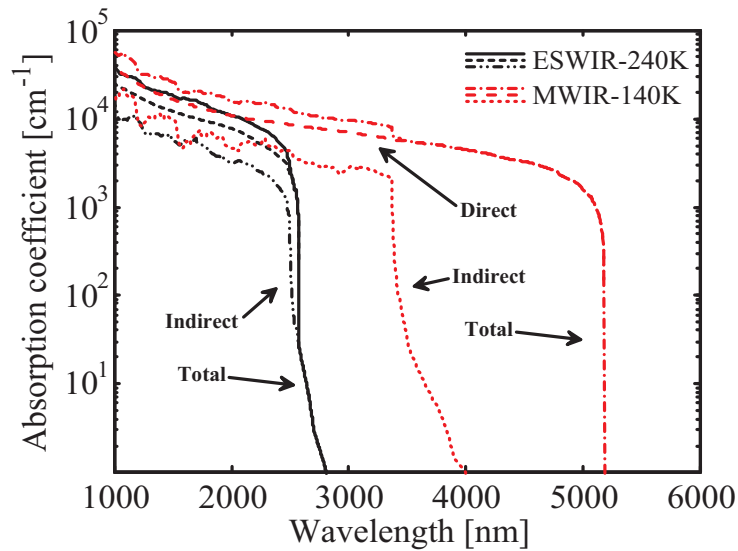
Figure 13: Absorption coefficient for $Ge_{0.91}Sn_{0.09}$ and $Ge_{0.82}Sn_{0.18}$ intrinsic semiconductors. The direct and indirect components have been separated.[45]
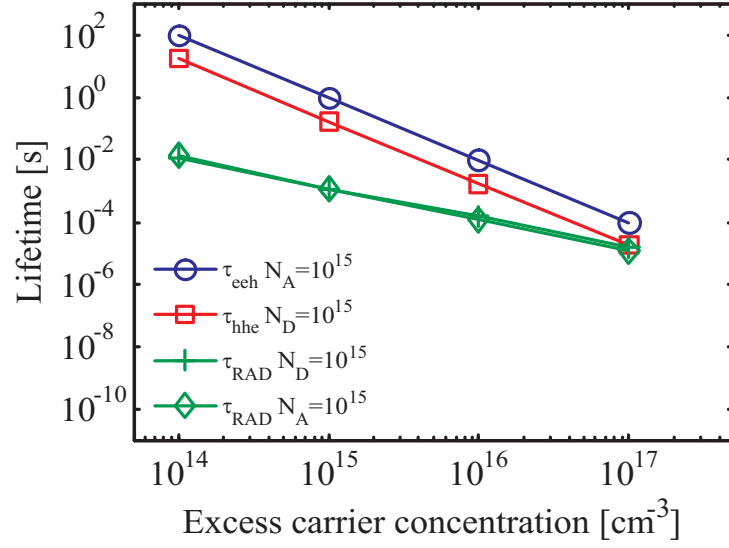
Figure 14: Radiative and Auger lifetimes for lightly doped (10^{15} cm^{-3}) Ge$_{0.91}$Sn$_{0.09}$ at 240 K. Doping has been considered of both types n and p. [45]
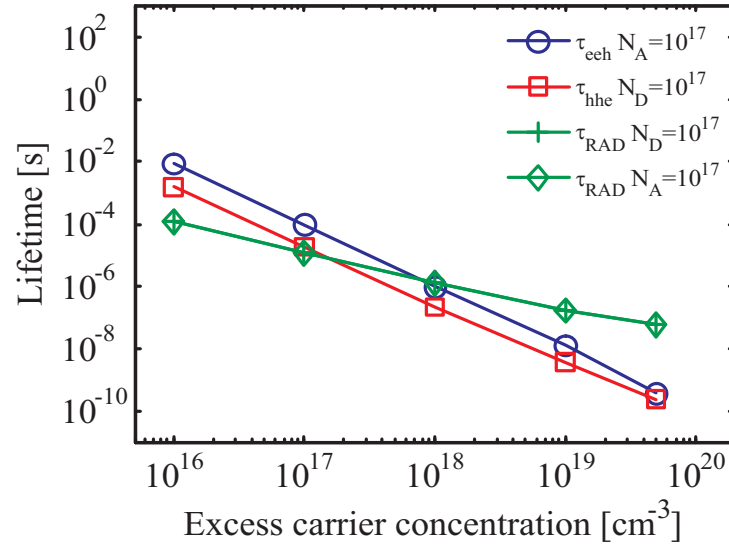
Figure 15: Radiative and Auger lifetimes for lightly doped (10^{17} cm^{-3}) Ge$_{0.91}$Sn$_{0.09}$ at 240 K. Doping has been considered of both types n and p.[45]
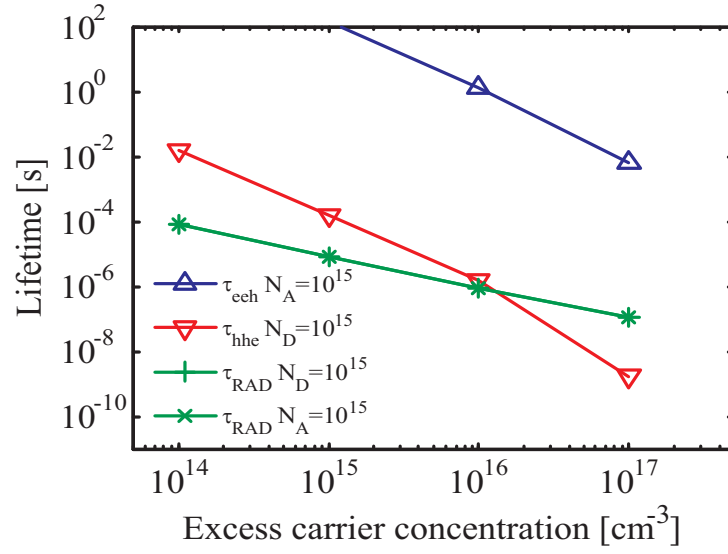
Figure 16: Radiative and Auger lifetimes for lightly doped (10^{15} cm^{-3}) Ge$_{0.82}$Sn$_{0.18}$ at 140 K. Doping has been considered of both types n and p.[45]
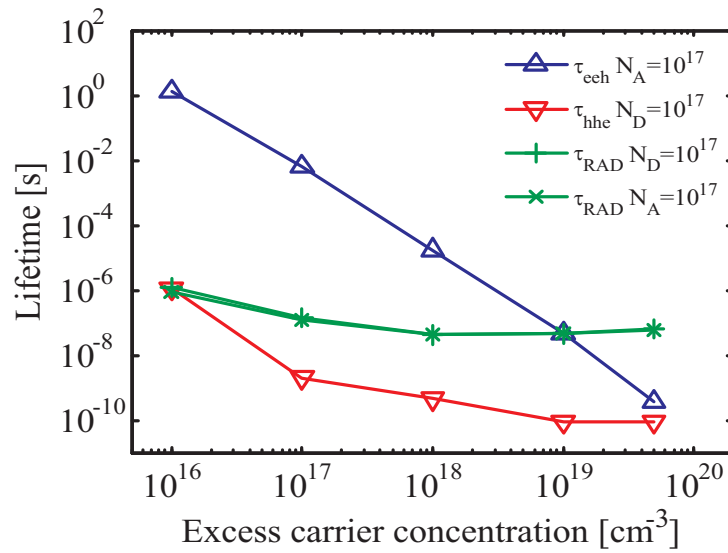
Figure 17: Radiative and Auger lifetimes for lightly doped (10^{17} cm^{-3}) Ge$_{0.82}$Sn$_{0.18}$ at 140 K. Doping has been considered of both types n and p.[45]
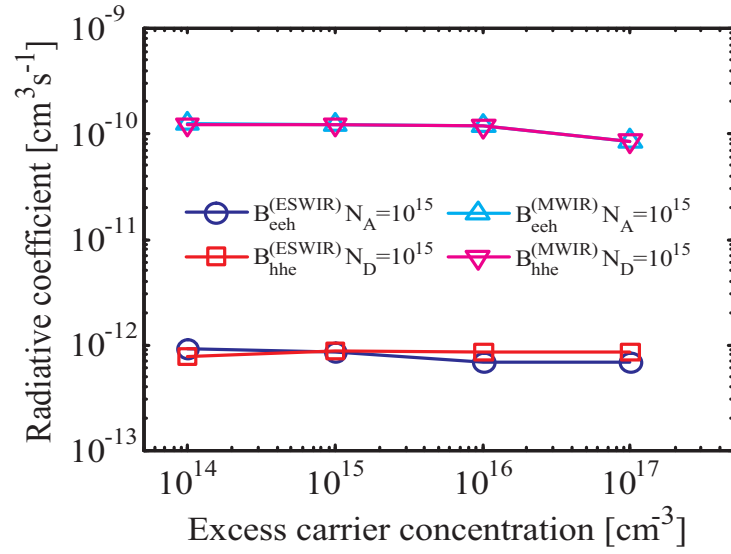
Figure 18: Radiative recombination coefficients for $Ge_{0.91}Sn_{0.09}$ and $Ge_{0.82}Sn_{0.18}$ for a doping concentration of 10^{15} cm^{-3} both n-type and p-type.[45]
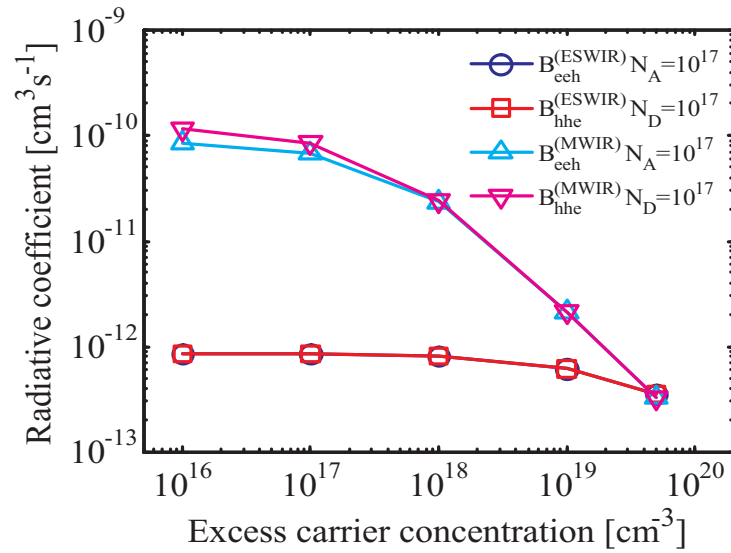
Figure 19: Radiative recombination coefficients for $Ge_{0.91}Sn_{0.09}$ and $Ge_{0.82}Sn_{0.18}$ for a doping concentration of 10^{17} cm^{-3} both n-type and p-type.[45]
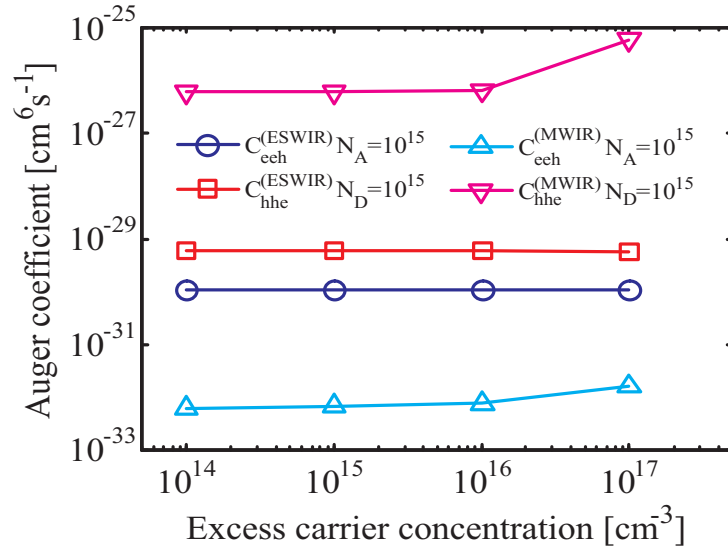
Figure 20: Auger recombination coefficients for $Ge_{0.91}Sn_{0.09}$ and $Ge_{0.82}Sn_{0.18}$ for a doping concentration of 10^{15} cm^{-3} both *n*-type and *p*-type.[45]
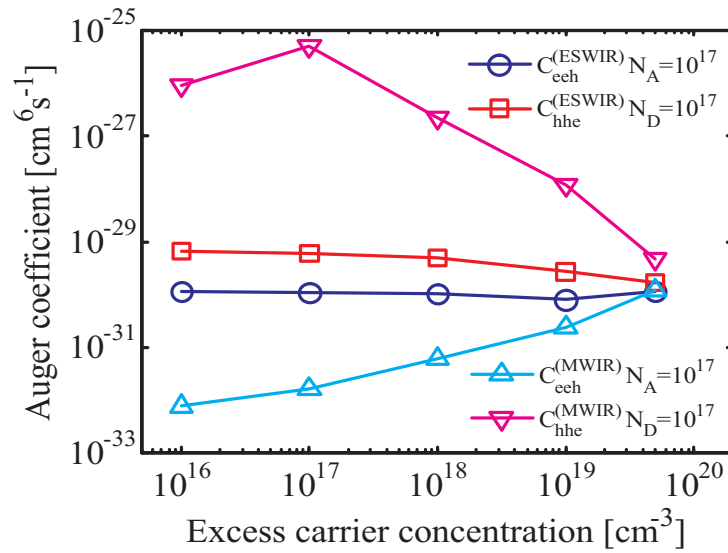
Figure 21: Auger recombination coefficients for $Ge_{0.91}Sn_{0.09}$ and $Ge_{0.82}Sn_{0.18}$ for a doping concentration of 10^{17} cm^{-3} both *n*-type and *p*-type.[45]

4

Conclusions

The Auger recombination properties of bulk germanium under different strain condition and the Auger and radiative recombination properties of bulk germanium-tin alloy in two configurations have been calculated.

The calculated Auger recombination properties of Ge could contribute to an effective design of IR light emitters, while the calculated optical and Auger recombination properties of $Ge_{1-x}Sn_x$, at two specific molar fractions, offered insight on the performance of this material as base material for infrared applications.

The irreducible wedge in the first Brillouin zone has been discretized with a non-uniform grid and a finer resolution around the relevant high symmetry points. The electronic band structure of relaxed and strained material have been numerically determined, over the discretized irreducible wedge, through an EPM code.

In order to calculate the Auger and radiative recombination rate, a Green's function based model has been applied to the full electronic band structure of Ge and $Ge_{1-x}Sn_x$. The Green's function based model included the electron-phonon interaction, from acoustic and non-polar optical phonons, and allowed to overcome the well known numerical limitations of second order perturbation theory. To the total radiative recombination rate, the contribution coming from transitions between first conduction band and the first and second valence bands have been considered. To the total Auger recombination rate, different combinations of initial and final states for the scattered particle have been considered, for electron up to the second conduction band and for hole up to the second valence band.

The calculation of Auger recombination coefficients in bulk relaxed and strained Ge at 300 K revealed that the dominant Auger recombination process for relaxed Ge is direct *hhe*. However, the application of a biaxial tensile strain deform the band structure and makes the direct *eeh* the dominant Auger mechanism. This result is in contrast with earlier analytic works. However, the advanced formalism and the absence of numerical and analytic simplifications in this work represent a novelty and further experimental validations are required.

The germanium-tin alloy has been studied since the 1960 and posses characteristics that makes it suitable for the fabrication of optoelectronic devices operating in the infrared spectral range. However, device quality thin films have been achieved only recently and for low

Sn molar fraction. Furthermore, there is no uniform consensus on the basic electronic properties of this alloy.

The electronic band structure of bulk relaxed $Ge_{1-x}Sn_x$ has been determined with the EPM code in order to reproduce the average semiconductor energy gap function of molar fraction by tuning the disorder and spin disorder parameters. As a result, the transition from an indirect gap semiconductor to a direct gap semiconductor is detected at 11% Sn molar fraction and the effective mass for conduction and valence bands at critical points of reciprocal lattice have been calculated and reported.

To the calculation of Auger and radiative recombination properties, two cutoff wavelengths have been chosen, 2.7 μm (extended short wave) and 5.0 μm (mid wave), at 240 K and 140 K, respectively. The corresponding molar fractions are 9% at 2.7 μm and 18% 5.0 μm.

The absorption coefficient have been calculated for both $Ge_{0.91}Sn_{0.09}$ and $Ge_{0.82}Sn_{0.18}$. Results revealed an absorption edge close to the cutoff wavelength due to phonon-assisted transitions for $Ge_{0.91}Sn_{0.09}$, while a sharp absorption edge, from direct processes, is detected for $Ge_{0.82}Sn_{0.18}$. These results confirmed the indirect energy gap nature of $Ge_{0.91}Sn_{0.09}$ and the direct energy gap of $Ge_{0.82}Sn_{0.18}$.

The radiative and Auger lifetimes and recombination coefficients have been calculated for $Ge_{0.91}Sn_{0.09}$ and $Ge_{0.82}Sn_{0.18}$ given four different doping configurations: *n*-type doping of 10^{15} cm^{-3}, *n*-type doping of 10^{17} cm^{-3}, *p*-type doping of 10^{15} cm^{-3}, *p*-type doping of 10^{17} cm^{-3}.

The radiative and Auger lifetimes determined the competition between the two recombination mechanisms. Results reported that Auger recombinations are suppressed for the case of *p*-doped $Ge_{0.82}Sn_{0.18}$, while the doping type has a small impact on radiative and Auger processes in $Ge_{0.91}Sn_{0.09}$. Furthermore, the doping type does not impact on the radiative recombination processes in both $Ge_{0.91}Sn_{0.09}$ and $Ge_{0.82}Sn_{0.18}$.

The Auger and radiative recombination coefficients have been calculated in order to be used in device simulations and are constant up to excess carrier concentrations of 10^{18} cm^{-3} for $Ge_{0.82}Sn_{0.18}$, while remain constant at all excess carrier concentrations for $Ge_{0.91}Sn_{0.09}$.

Part II

Numerical simulation of GaN based light emitting diodes

Introduction

During the last decade, GaN/InGaN based light emitting diodes (LED) were the subject of an intense research activity. The strong point of GaN/InGaN based light emitting diodes is in the capability of tuning the emission wavelength by a fine control over the incorporated indium molar fraction during the fabrication process, which allow to cover the entire range of visible spectrum. These devices have already saturated the entertainment market and are slowly becoming part of the general illumination market.

One of the most controversial and debated issue of these devices has been the *droop*.[115] This phenomena consists in a reduction of internal quantum efficiency when the injected current density overcome a threshold value at which the optical emitted power reaches its maximum.[17, 115] This phenomena represent a limiting factor to the maximum optical power that can be achieved at the optimal working point, where the internal quantum efficiency (IQE) is maximized.[28, 63]

A number of solutions have been proposed in order to limit the effects of *droop*. The use of multi-quantum-well structures, in which carriers escaping from the first quantum well would be recaptured and radiatively recombined in the remaining quantum wells.[33] The use of non-conventional patterns for the mesa contact in order to suppress current crowding features and improve carrier redistribution along the plane perpendicular to transport.[73, 119] However, a *droop* free device is still impossible to fabricate and the adopted solutions allowed to optimize, rather than improve, the IQE of LEDs.

The research effort up to now led to the identification of Auger recombinations as the physics mechanism underlying the *droop* phenomena.[6, 19, 22–26] Due to their intrinsic nature, Auger recombinations cannot be suppressed by improving material quality. Therefore, the *droop* phenomena will always impose an upper limit to the performances of GaN/InGaN LED devices.

Another mechanism that can severely undermine the performances of GaN/InGaN LED devices is the so called *thermal droop*. The *thermal droop* phenomena refers to the decrease in optical power with increasing temperature, which may lead to remarkable optical losses. Many research groups found experimental evidence of this phenomena. Huh *et al.*[60] investigated the effect of temperature on electrical and optical performances of MQW LEDs with different compositions in the active region and concluded that the presence of a *p*-doped

AlGaN electron blocking layer (EBL) could reduce the optical losses with increasing temperature. Lee *et al.*[69] investigated the impact of different substrate thicknesses on the junction temperature of MQW LED mesa devices proving that thinner substrates improve thermal dissipation, effectively reducing the junction temperature. Meyaard *et al.*[83] investigated the impact of different mesa sizes in MQW LED devices and detected that the larger the chip size, the faster the device performances degrade with increasing temperature. However, very little is known about the physics based mechanism underlying the *thermal droop* phenomena.

Despite the experimental effort, the physical processes responsible for this effect have not been identified yet. Therefore, this part is devoted to the device modeling of GaN/InGaN based LED devices, in an attempt to improve the insight toward the physical processes underlying the *thermal droop* phenomena. More specifically, this work is part of a bigger collaboration, culminated with the paper published by De Santi *et al.*[43], in which the impact on the device IQE of different physics based processes with temperature is studied. Within this framework, this work investigates the impact on the IQE of Shockley-Read-Hall recombination phenomena with temperature.

After this brief introduction, three more chapters will follow. Chapter 6 will report on the physics based models and the numerical simulation methodologies adopted to tackle the problem, then chapter 7 will present and discuss results. Finally, chapter 8 will draw conclusions.

Device and physics based models

6.1 DEVICE STRUCTURE

The device under study is a light emitting diode device grown on Si substrate and fabricated by OSRAM Licht AG. The device can be viewed as a stack of layers: a 2.0 µm thick n-doped GaN buffer, doped $5 \cdot 10^{18}$ cm^{-3}, a 8 nm thick intrinsic GaN barrier, a 2.5 nm thick In$_x$Ga$_{1-x}$N quantum well at 18% molar fraction,[97] a 2 nm thick intrinsic GaN spacer, a 40 nm thick p-doped Al$_x$Ga$_{1-x}$N electron blocking layer (EBL) at 15% molar fraction, doped $2.0 \cdot 10^{19}$ cm^{-3}, and a 150 nm thick p-doped GaN capping layer, doped $2.0 \cdot 10^{19}$ cm^{-3}. The stack of layers for the device has been reported in Fig.22 and details on doping concentration, type, and activation energy have been reported in Tab.4.

The intrinsic layers (namely 2 and 3) are characterized by an n-type background doping concentration of 10^{16} cm^{-3}. The background n-type doping concentration results from the unwanted incorporation of donor impurities - probably silicon or oxygen - during the crystalline growth.[91, 92] The activation energies for the dopant species represent the energy shift from the conduction and valence band edges for donor and acceptor dopants respectively.

The doping concentration profiles are not abrupt at the interface between two materials. Instead, dopants are assumed to diffuse in nearby regions. The diffusion tail is assumed to have a Gaussian decaying behavior characterized by a standard deviation of 1Å, as depicted in Fig.23.

The area of the device active region is 250 µm×250 µm. This information allow us to scale all current related data from A to A/cm^2.
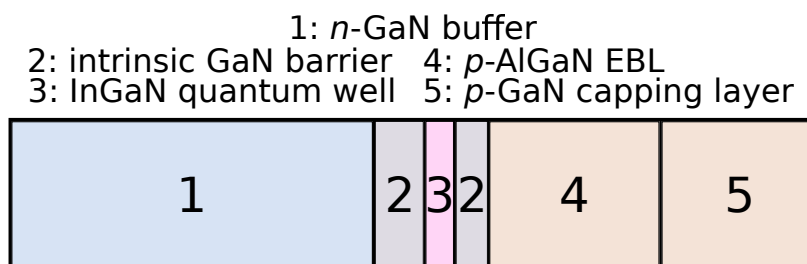
Figure 22: Stack of layers in investigated LED device.

The exact geometry of the device is not known in its entirety. However, numerical simulations of charge transport are monodimensional
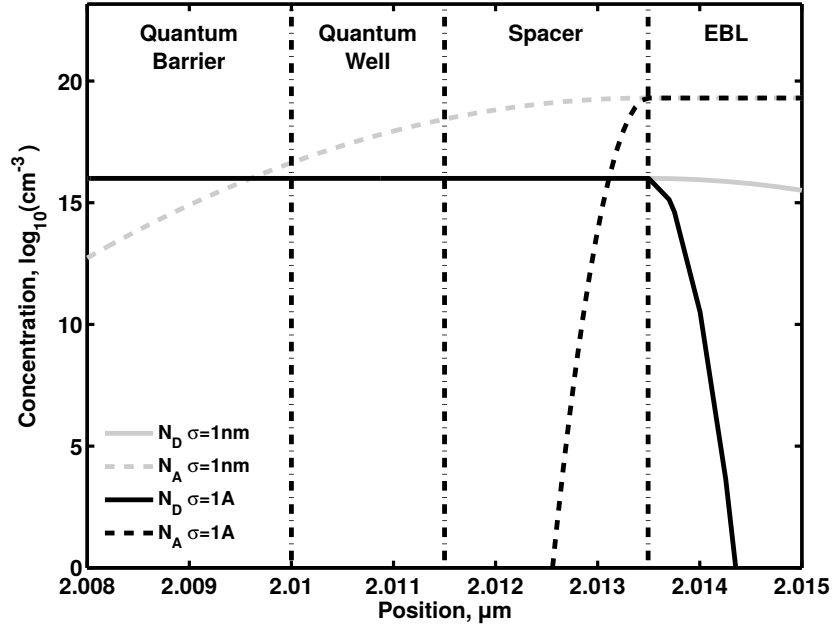
Figure 23: Comparison between different doping profile diffusions in the device active region. The diffusion profile at the interface between GaN Spacer and AlGaN EBL has a Gaussian decaying behavior with standard deviation of $\sigma = 1\,nm$ and $\sigma = 1\text{Å}$.

along the dimension of crystal growth since, from manufacturing specifications, the device is assumed vertical and charge transport is assumed to take place only along one direction. The simulation line crosses all device interfaces perpendicularly, from region 1 to 5, in reference to Fig.22. The electrical contacts are placed at the extremal points of the simulation line: the ending points of region 1 and of region 5. An in scale representation of the device active region has been given in chapter 7 through its band diagram close to flat-band condition (Fig.35).

#	Layer	Thickness, nm	N, cm^{-3}	E$_a$, meV
5	p-GaN cap	150	$2 \cdot 10^{19}$	200
4	p-AlGaN EBL	40	$2 \cdot 10^{19}$	200
2	n-GaN	2	$1 \cdot 10^{16}$	20
3	n-InGaN QW	1.5	$1 \cdot 10^{16}$	20
2	n-GaN	10	$1 \cdot 10^{16}$	20
1	n-GaN	2000	$5 \cdot 10^{18}$	20

Table 4: Table reporting the doping type, concentration (N), activation energy (E$_a$) and thickness of each layer composing the device in reference to the numbers (#) given in Fig.22.

6.2 CHARGE TRANSPORT MODEL

The commercial tool Crosslight APSYS$^{©}$ has been used to perform charge transport simulations in InGaN/GaN based LED device reported in Fig:22.

6.3 NUMERICAL MODEL FOR THE CHARGE TRANSPORT PROBLEM

The problem of charge transport has been numerically solved by adopting an improved drift-diffusion simulation scheme available in Crosslight APSYS$^{©}$. The improved simulation scheme takes into account the quantization effects localized in the device active region.

The semi-classical drift-diffusion simulation scheme involves the numerical resolution of the non-linear system of equation composed by the Poisson's equation, the continuity equation for electron and hole, and the drift-diffusion equation for electron and hole current densities:[98]

$$
\begin{cases}
\nabla \left(\varepsilon \left(\mathbf{r} \right) \nabla \phi \left(\mathbf{r} \right) \right) = -\frac{q}{\varepsilon_0} \rho \left(\mathbf{r} \right) \\
\frac{\partial n(\mathbf{r},t)}{\partial t} = \frac{1}{q} \nabla \mathbf{J}_n \left(\mathbf{r}, t \right) + G_n \left(\mathbf{r}, t \right) - R_n \left(\mathbf{r}, t \right) \\
\frac{\partial p(\mathbf{r},t)}{\partial t} = -\frac{1}{q} \nabla \mathbf{J}_p \left(\mathbf{r}, t \right) + G_p \left(\mathbf{r}, t \right) - R_p \left(\mathbf{r}, t \right) \\
\mathbf{J}_n \left(\mathbf{r}, t \right) = qn \left(\mathbf{r}, t \right) \mu_n \left(\mathbf{r} \right) \mathbf{E} \left(\mathbf{r}, t \right) + qD_n \left(\mathbf{r} \right) \nabla n \left(\mathbf{r}, t \right) \\
\mathbf{J}_p \left(\mathbf{r}, t \right) = qp \left(\mathbf{r}, t \right) \mu_p \left(\mathbf{r} \right) \mathbf{E} \left(\mathbf{r}, t \right) - qD_p \left(\mathbf{r} \right) \nabla p \left(\mathbf{r}, t \right)
\end{cases}
\tag{33}
$$

In Eq.33,$\varepsilon \left(\mathbf{r} \right)$ is the relative permittivity, $\phi \left(\mathbf{r} \right)$ is the electrostatic potential, $\rho \left(\mathbf{r} \right)$ is the net-charge concentration, $n \left(\mathbf{r}, t \right)$ and $p \left(\mathbf{r}, t \right)$ are the electron and hole concentrations, $\mathbf{J}_n \left(\mathbf{r}, t \right)$ and $\mathbf{J}_n \left(\mathbf{r}, t \right)$ are the electron and hole current densities, $D_n \left(\mathbf{r} \right)$ and $D_p \left(\mathbf{r} \right)$ are the electron and hole diffusion coefficients, and $\mu_n \left(\mathbf{r} \right)$ and $\mu_p \left(\mathbf{r} \right)$ are the electron and hole mobility terms. The equation system reported in Eq.33 cannot be solved in a close form. Therefore, self-consistent numerical procedures are required. A viable numerical approach to solve this system has been given by Scharfetter[95] and Gummel[54]. In their approach, they discretize the device according to a finite difference scheme and perform two cardinal assumptions: the electron and hole carrier concentrations are function of the electrostatic potential and follow an exponential behavior, while the electrostatic potential varies linearly between adjacent nodes of the finite discretization grid. Under these assumptions, the system of equations became numerically stable and the calculated electron and hole concentration across the device do not show oscillatory behaviors. Finite elements approaches to the resolution of the above system of equations have bee proposed. However, finite elements are scarcely used due to an increased numerical burden originating from the requirement of high

order basis functions.[13, 90] Eventually, solutions to the discretized non-linear system of equations (Eq.33) are found through the application of a Newton or Newton-like method.[8–11] The self-consistent procedure starts with an estimate of the electrostatic potential across the device. Given the electrostatic potential profile, the electron and hole concentration are calculated along the device. The calculated carrier concentrations are plugged into Poisson's equation, which is self-consistently solved for the electrostatic potential. The procedure is iterated until the difference between the calculated carrier concentrations for two consecutive iterations are smaller than a chosen value.

The improved drift-diffusion scheme model quantization effects in the active region of the device. The improved scheme adds the Schrödinger equation to the system of equations in Eq.33 that depends on the electrostatic potential and returns an additional charge density. The most general form for the considered Schrödinger equation is an eigenvalue problem of the form

$$\left[\hat{H}\left(\mathbf{r},\mathbf{k}\right)+\hat{V}\left(\mathbf{r}\right)\right]\Psi\left(\mathbf{r},\mathbf{k}\right)=E\left(\mathbf{r},\mathbf{k}\right)\Psi\left(\mathbf{r},\mathbf{k}\right), \tag{34}$$

in which $\hat{H}\left(\mathbf{r},\mathbf{k}\right)$ is the Hamiltonian for the system, $\Psi\left(\mathbf{r},\mathbf{k}\right)$ are the eigenvectors, or wavefunctions, $E\left(\mathbf{r},\mathbf{k}\right)$ are the eigenvalues, or quantized energy levels, and $\hat{V}\left(\mathbf{r}\right)$ correspond to the position dependent potential energy of the system.

In the improved simulation scheme, the Schrödinger equation, expressed in the $\mathbf{k}\cdot\mathbf{p}$ approximation, is coupled to the Poisson's equation. The term $\hat{V}\left(\mathbf{r}\right)$ in Eq.34 correspond to the electrostatic potential $\phi\left(\mathbf{r}\right)$ in first line of Eq.33 and from the eigenfunctions of Eq.34 a charge density contribution is calculated and plugged in the right-hand-side term of Poisson's equation. Therefore, the electrostatic potential is updated, at each step of the iteration procedure, through a self-consistent resolution of Poisson's equation to Schrödinger equation. This problem is well known in literature as the coupled Poisson-Schrödinger problem.[65, 76, 112]

In the framework of a monodimensional numerical simulation of carrier transport in Crosslight APSYS©, the *self-consistent QW* model with valence mixing has been adopted in order to include quantization effects into the active region.[42]

In order to solve the Poisson-Schrödinger problem only in the active region of the device, the software allows the user to choose the size of a *quantum box*. The *quantum box* is defined as a framed portion of the device over which the Poisson's equation is coupled to the Schrödinger equation. It is selected in order to be symmetric with respect the center of the quantum well and to include the quantum barrier. The Schrödinger equation defined over the quantum box is formulated in the $\mathbf{k}\cdot\mathbf{p}$ approach and discretized along the direction perpendicular to the quantum well plane. The boundary conditions of the Schrödinger equation at the quantum box boundaries are are

Dirichlet type and implement an infinite potential barrier. An analysis on the most proper size for the quantum box has been performed in Chap.7

The software computes the self-consistent carrier concentration resulting from the resolution of Poisson-Schrödinger problem as[42]

$$n_{2D}\left(\mathbf{r}_\parallel, \mathbf{r}_\perp\right) = \sum_j \Psi_j\left(\mathbf{r}_\perp\right) \rho_j^{(0)} k_b T \ln\left\{1 + \exp\left[\frac{E_f\left(\mathbf{r}_\parallel, \mathbf{r}_\perp\right) - E_j}{k_b T}\right]\right\},$$

(35)

where the summation runs over the quantized levels of index j, $\mathbf{r}_\parallel$ is the direction parallel to the quantum well plane, $\mathbf{r}_\perp$ is the direction perpendicular to the quantum well plane. $\Psi_j\left(\mathbf{r}_\perp\right)$ is the eigenfunction of the j-th state, and $E_f\left(\mathbf{r}_\parallel, \mathbf{r}_\perp\right)$ is the quasi-Fermi level for electron or hole population.

In the quantum box, the Hamiltonian term in the Schrödinger equation correspond to the $\mathbf{k}\cdot\mathbf{p}$ Hamiltonian given by Chuang.[37] The set of $\mathbf{k}\cdot\mathbf{p}$ simulation parameters used in this work for the quantum box region have been taken from the work of Calciati *et al.*.[33]

In order to perform charge transport simulations a number of physics based variables have to be properly modeled. The following sections report on parameters and models for the semi-classical drift-diffusion simulation.

6.3.1 *Coupling QW model with continuity equation*

Once the self-consistent solution of Poisson-Schrödinger problem is achieved, the confined electron and hole populations are known.[42] However, the software manual doesn't report any further information on the numerical technique adopted to solve continuity equations into the quantum well region.

A sane treatment of the problem would split the carrier concentration into the quantized region in a sum of two populations: bounded and free charges. The bounded charge results from the solution of Poisson-Schrödinger problem, while the free charge would come from the resolution of continuity equations. In solving the continuity equations, only states at energies above the bulk band edges would have to be considered in the quantized region, and boundary conditions at the QW interfaces would be required to ensure the continuity of free carrier populations through the device.

In absence of further information regarding the real implementation, this digression remains speculative.

6.3.2 *Incomplete ionization model*

Due to the high energy gap of GaN and $Al_xGa_{1-x}N$, an accurate estimation of the ionized acceptor and donor concentrations is fundamental.[53, 66, 93] The activation energy for a given dopant is considered as the absolute value of the energy difference between the dopant energy level in the gap and the correlated band edge. Being E_D and E_A the donor and acceptor activation energies, the ionized doping concentration is given as[42]

$$N_D^+ = \frac{N_D}{1 + g_D e^{\frac{F_n - E_D}{k_b T}}}, \qquad N_A^- = \frac{N_A}{1 + g_A e^{\frac{E_A - F_p}{k_b T}}}. \tag{36}$$

In Eq.36, g_D and g_A are the degeneracy number for donors and acceptors, while F_n and F_p are the quasi-Fermi levels for electron and hole, respectively. The degeneracy of donors and acceptors is automatically set to $g_D = 4$ and $g_A = 2$ by the software.

6.3.3 *Effective mass*

The modeling of the effective mass for electron and hole is of vital importance in device level simulation. In the bulk regions the effective mass is assumed to be isotropic. Furthermore, due to the band structure characteristics of GaN, $In_xGa_{1-x}N$, and $Al_xGa_{1-x}N$ the carrier transport is assumed to take place only around the minimum of Γ valley.

In case of bulk regions, constant values for the isotropic effective mass of electron and hole have been used and their values have been reported in Tab.6.

A effective density of states for conduction and valence states has been defined according to

$$N_{c|v}(T) = 2 \left(\frac{2\pi k_b m_{e|h} T}{\hbar^2} \right)^{\frac{3}{2}} = 2.54 \cdot 10^{19} \left(\frac{m_{e|h} T}{300 m_0} \right)^{\frac{3}{2}}, \tag{37}$$

in which, m_0 is the electron mass at rest, and $m_{e|h}$ is the effective mass for electron or hole.

6.3.4 *Carrier occupation statistics and free carrier model*

The transient simulation performed on the device lead the device out of thermal equilibrium up to a point where the Maxwell-Boltzmann distribution cannot be used to describe the occupation statistic of electron and hole. Therefore, the use of Fermi-Dirac distribution is mandatory and the electron and hole free carrier concentrations have been calculated according to

$$n = N_c(T) \int_{E_c}^{+\infty} \frac{\sqrt{E}}{1 + e^{\frac{E - (E_c - F_n)}{k_b T}}} dE, \quad p = N_v(T) \int_{-\infty}^{E_v} \frac{\sqrt{E}}{1 + e^{\frac{E - (E_v - F_p)}{k_b T}}} dE,$$

$$(38)$$

in which, F_n and F_p are the quasi-Fermi levels for electron and hole.

6.3.5 *Band gap model*

The energy gap is temperature dependent according to the model proposed by Varshni:[114]

$$E_g\left(T\right) = E_{g0} - \alpha \frac{T^2}{\beta + T},$$

$$(39)$$

in which α and β are parameters fitting the temperature dependent measurements on the energy gap. The parameters for $In_{0.18}Ga_{0.82}N$ and $Al_{0.15}Ga_{0.85}N$ have been taken as a linear interpolation in the molar fraction of values for GaN, InN, and AlN given in the work of Calciati *et al.*.[33] For the $In_{0.18}Ga_{0.82}N$ and $Al_{0.15}Ga_{0.85}N$ regions a band offset of 60/40 has been used to align the band diagrams.

6.3.6 *Carrier mobility model*

The electron and hole mobility is a parameter that directly enters drift-diffusion equations (Eq.33) and enters the Einstein diffusivity coefficient as $D_{n|p} = \mu_{n|p} q k_B T$. The temperature dependent mobility model is given as[75]

$$\mu_{n|p}\left(T\right) = \mu_{n|p}\left(\frac{300}{T}\right)^{\alpha_{n|p}},$$

$$(40)$$

in which $\mu_{n|p}$ is the pure lattice mobility and $\alpha_{n|p}$ is a parameter that has been set to 3/2 for both electron and hole. Values for the pure lattice mobility constant used in the simulation have been reported in Tab.5.

6.3.7 *Heterojunction model*

The heterojunctions in the device are localized at $GaN/In_{0.18}Ga_{0.82}N$ and $GaN/Al_{0.15}Ga_{0.85}N$ interfaces and a thermionic emission model is applied to each one of them, as reported in[42, 106, 131]. The thermionic emission model in the software defines the current fluxes across the junction as[42]

$$J_n = \gamma_n \nu_{bn}\left(n_b - n_{b0}\right), \qquad J_p = \gamma_p \nu_{bp}\left(p_b - p_{b0}\right), \qquad (41)$$

where γ_n and γ_p are parameters set to 1 in this work, n_b and p_b denote the electron and hole concentrations on the barrier side of the junction, n_{b0} and p_{b0} are the concentrations when the quasi-Fermi

levels are the same as those on the opposite side of the barrier, and v_{bn} and v_{bp} are the thermal recombination velocities given as

$$v_{bn} = \sqrt{\frac{k_b T}{2 m_{bn} \pi}}, \qquad v_{bp} = \sqrt{\frac{k_b T}{2 m_{bp} \pi}} \tag{42}$$

in which m_{bn} and m_{bp} are the electron and hole effective mass on the side of the barrier, respectively. The thermionic emission conditions at heterojuctions impose a zero net-current density across the heterointerface ensuring the continuity of quasi-Fermi levels.

6.3.8 *Polarization charges at heterointerfaces*

In addition to the high spontaneous polarization characteristics of GaN, GaN/In$_{0.18}$Ga$_{0.82}$N and GaN/Al$_{0.15}$Ga$_{0.85}$N heterointerfaces are characterized by a strong strain induced by the difference in the lattice constants on the two sides of the heterointerface.[3, 4, 18, 48] The spontaneous and piezoelectric polarization charge is of fundamental importance in the modeling of GaN-based devices. It induces the so called *quantum confinement Stark effect* improving carrier confinement in quantum well structures.[72] Furthermore, the piezoelectric polarization vector at the heterointerfaces of GaN based devices is quadratically dependent on strain, as reported by Fiorentini *et al.*.[48]

The heterointerfaces of the devices simulated in this work are planar in the *xy* plane. Therefore, the spontaneous and piezoelectric polarization vectors have been defined only in the *z* direction as

$$\varepsilon(x) = \frac{a_{GaN} - a_{Y_x Ga_{1-x} N}}{a_{Y_x Ga_{1-x} N}}, \tag{43}$$

$$P_{GaN}^{PZ} = P_{GaN}^{(0)} \varepsilon(x) + P_{GaN}^{(1)} \varepsilon(x)^2, \tag{44}$$

$$P_{YN}^{PZ} = P_{YN}^{(0)} \varepsilon(x) + P_{YN}^{(1)} \varepsilon(x)^2, \tag{45}$$

$$P_{Y_x Ga_{1-x} N}^{PZ} = P_{GaN}^{PZ} x + P_{YN}^{PZ} (1-x), \tag{46}$$

$$P_{Y_x Ga_{1-x} N}^{SP} = P_{YN}^{SP} x + P_{GaN}^{SP} (1-x) + P_{b(YN)}^{SP} x (1-x), \tag{47}$$

$$P_z = -\alpha \left(P_{Y_x Ga_{1-x} N}^{SP} + P_{Y_x Ga_{1-x} N}^{PZ} \right), \tag{48}$$

where, a_{GaN} and $a_{Y_x Ga_{1-x} N}$ are the lattice constant of the substrate and of the alloy, P^{PZ} stands for the piezoelectric polarization vector, P^{SP} stands for the spontaneous polarization vector, α is a tunable parameter representing the degree of relaxation of the interface and used to fit experimental data, and the sign in Eq.48 is given by the surface polarization at the interface, induced during the crystalline growth.[120] The spontaneous and piezoelectric polarization coefficients that have been used in the simulation are reported in Tab.5.

The position dependent polarization charge density is computed from the total polarization vector as

$$q_{pc}(\mathbf{r}) = -\nabla \mathbf{P}(\mathbf{r}). \tag{49}$$

6.3.9   *Radiative and non-radiative recombination models*

The radiative recombination rate is computed differently in the bulk regions and in the quantum box region. In the bulk region, the radiative recombination rate is computed as

$$R_{RAD} = B\left(np - n_i^2\right), \tag{50}$$

where B is the radiative recombination coefficient, n and p are the free carrier concentrations, and n_i is the intrinsic carrier concentration. On the other hand, the radiative recombination rate in the quantum box is computed according to the first order perturbation theory as[38, 43]

$$R_{RAD} = \sum_{i,j} \int_0^\infty \left(\frac{q^2 n \hbar\omega}{m_0^2 \varepsilon_0 \pi \hbar^2 c^3}\right) \left|M_{ij}\right|^2 f_j\left(1 - f_i\right) \rho_{ij} L\left(\hbar\omega\right) d\hbar\omega, \tag{51}$$

where q is the elementary charge, n is the quantum well refractive index, m_0 is the electron mass, ε_0 is the vacuum permittivity, c is the speed of light in vacuum, M_{ij} is the matrix element measuring the dipole strength between states i and j, f_i and f_j are the Fermi-Dirac occupation statistics, ρ_{ij} is the 2D joint density of states for states i and j, and $L\left(\hbar\omega\right)$ is a Lorentzian distribution accounting for the energy broadening of the emission spectrum.

The Lorentzian distribution term in Eq.51 is given as

$$L\left(\hbar\omega\right) = \frac{1}{\pi} \frac{\hbar\gamma}{\left(E_{ij} - \hbar\omega\right)^2 - \left(\hbar\gamma\right)^2}, \tag{52}$$

where E_{ij} is the energy difference between the states i and j participating in the transition and $\hbar\gamma = \hbar/\tau$ is half of the Lorentzian line width, for which the lifetime τ has been set to 0.1 ps.[38]

The non-radiative recombination rates in the device are of two types: Shockley-Read-Hall (SRH) recombinations due to trap states and Auger recombinations. The Auger recombination rate is computed according to

$$R_{AUG} = \left(C_n n + C_p p\right)\left(np - n_i^2\right), \tag{53}$$

in which C_n and C_p are the Auger recombination coefficients for electron and hole expressed in $cm^6 s^{-1}$.

The Shockley-Read-Hall recombination process is an extrinsic recombination mechanism mediated by state traps into the energy gap. This type of recombinations dominates in low injection regime where the current density is characterized mainly by diffusion processes, while radiative and Auger recombinations are negligible. Furthermore, this type of recombinations are well known as a performance limiting factor in photodetector devices.[7] Nonetheless, the presence of trap states in the energy gap foster transport mechanisms such

as trap-assisted tunneling (TAT) that correctly describe sub-threshold features of current-voltage characteristic in forwardly biased GaN-based LED devices.[27, 78–80]

The SRH recombination rate is computed according to[101, 103, 113]

$$R_{net}^{SRH} = \frac{np - n_i^2}{\tau_p(n + n_1) + \tau_n(p + p_1)}, \tag{54}$$

in which n and p are the electron and hole concentrations, n_i is the intrinsic carrier concentration, τ_n and τ_p are the electron and hole lifetimes. The values of n_1 and p_1 correspond to electron and hole concentrations calculated when the quasi-Fermi energy is equal to the trap energy E_t.

Eq.54 can be recast in another form

$$
\begin{aligned}
R_n^{SRH} &= c_n n N_t (1 - f_t) - c_n n_1 N_t f_t, \\
R_p^{SRH} &= c_p p N_t (1 - f_t) - c_p p_1 N_t f_t, \\
R_{net}^{SRH} &= R_n^{SRH} - R_p^{SRH},
\end{aligned}
\tag{55}
$$

in which N_t is the trap density, f_t is the trap occupation probability, and c_p and c_n are the capture rates, related to the trap density and capture cross section by

$$\frac{1}{\tau_{n|p}} = c_{n|p} N_t, \qquad c_{n|p} = \sigma_{n|p} v_{n|p}, \tag{56}$$

in which $\tau_{n|p}$ is the SRH lifetime, $\sigma_{n|p}$ is the capture cross section, and $v_{n|p}$ are the carrier thermal velocities.

The software Crosslight APSYS© implements the formulation reported in Eq.55. Furthermore, in this work the carrier lifetime is assumed to be temperature dependent according to[96]

$$\tau_{n|p}(T) = \tau_{n|p}(300) \left(\frac{300}{T}\right)^{\frac{3}{2}}, \tag{57}$$

which is an expression valid when the condition $k_b T \ll \hbar \omega_0$ is verified. This condition holds for all the simulations performed in this work since the phonon energy ($\hbar \omega_0$) is assumed to be 89 meV at 84K for the device under analysis, as given by Mandurrino *et al.*.[79, 80]

Numerical simulations and results

7

This chapter covers the methodology adopted to perform device level simulations. A reference framework has been established by obtaining a preliminary agreement on the electrical behavior of real and simulated device. Within the established reference framework, the impact of SRH recombination mechanism on the optical response of the device has been calculated. Finally, results from numerical simulations have been compared to experimental data and signatures of thermal droop phenomena have been discussed.

7.1 NUMERICAL SIMULATION METHODOLOGY

The power of numerical simulations lies in their ability to accurately predict the electrical behavior of a given device at the operating point. In order to do this, a preliminary agreement on the electrical behavior of real and simulated device has to be achieved.

The thickness of the quantum well has been cross-checked with experimental data and the size of the quantum box encompassing the device active region has been set. In order to check the quantum well thickness, experimental data on ambient temperature electroluminescence spectroscopy, reported in Fig.24, have been used. Finally, in reference to the case of a symmetric quantum well, the quantum box has been extended two nanometers outside the quantum well, in order to properly account for the effect of GaN barriers in $\mathbf{k} \cdot \mathbf{p}$ calculations for eigenenergies and eigenfunctions.

7.1.1 *Quantum well thickness*

The quantum well thickness has been experimentally measured with a degree of uncertainty. Secondary ion mass spectroscopy (SIMS) measurements determined the size of the quantum well according to the indium concentration profile in the device active region. Therefore, while the peak indium concentration in the quantum well can be estimated correctly, measurements on quantum well thickness are affected by statistical uncertainty.

In order to uniquely determine the thickness of the quantum well to be used in numerical simulations, a preliminary agreement with the peak wavelength given by experimental data on electroluminescence spectrum must be achieved. In fact, the thickness of the quantum well layer has a huge impact on the peak wavelength of electrolumines-

cence spectrum, as can be seen in Fig.24. On the other hand, parameters as the quantum box size and the amount of interface charge on the peak wavelength have been investigated and their impact on the peak wavelength of emission spectrum have been found negligible.

Transient simulations ramping injected current from $0\,A$ up to $10\,mA$ have been performed and a comparison between the normalized experimental and simulated electroluminescence spectrum determined that the quantum well thickness required to align the peak wavelength of real and simulated device is $1.5\,nm$, as depicted in Fig.24. Therefore, the total width of the quantum box has been set to $5.5\,nm$, which fully covers the quantum well and adjacent quantum barrier.
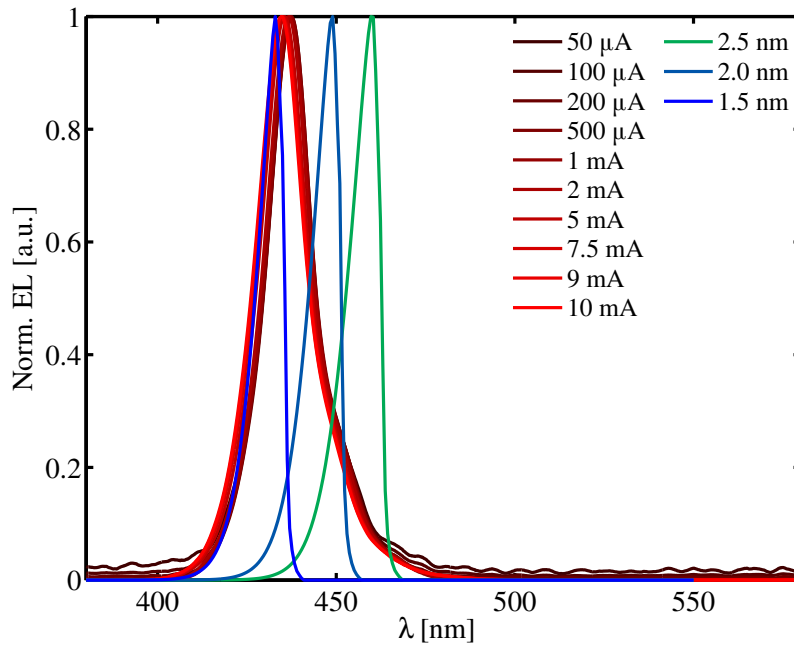
Figure 24: Experimental data on the normalized electroluminescence spectrum function of wavelength, at $300\,K$, of the SQW LED under different injection conditions and simulated electroluminescence spectrum at different quantum well thicknesses. Both simulated and measured EL spectrum have been normalized to unity. The peak wavelength of simulation results suggests a value of $1.5\,nm$ for the quantum well thickness.

7.1.2 *Analysis of experimental IV characteristics*

The charge transport simulations in this work consider only drift-diffusion processes as transport model and do not include auxiliary transport mechanisms, as trap-assisted tunneling or phonon-assisted tunneling. Therefore, the experimental current-voltage (IV) characteristics at different temperatures (Fig.25) must be fitted by numerical simulation results in a range of currents where the dominant transport mechanism is drift-diffusion. Therefore, the ideality coefficient

for the experimental IV characteristics at different temperatures has been calculated and related to the dominant transport mechanism.

Figure 25: Semilogarithmic plot of experimental data on current density versus applied bias for the device under analysis.
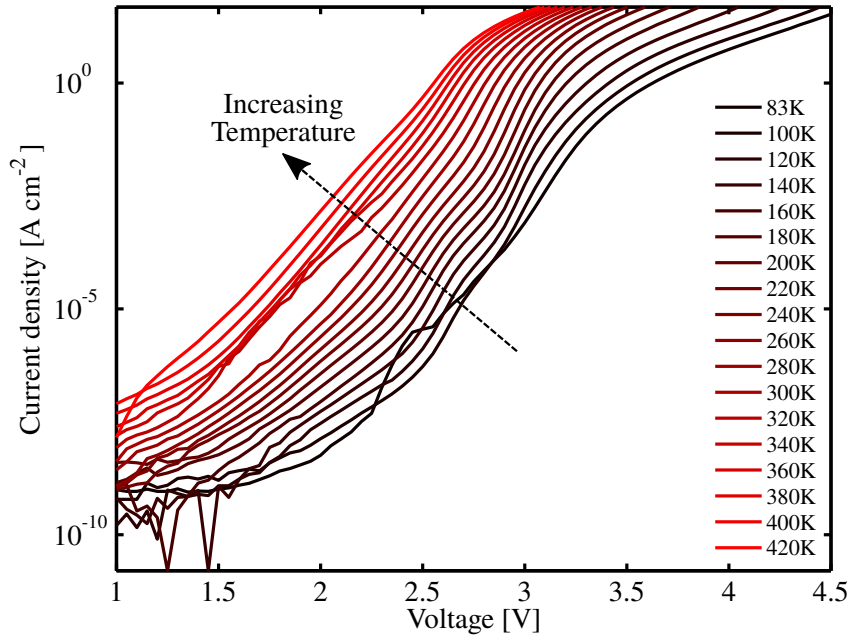
The ideality coefficient η is given as

$$\eta(V) = \frac{q}{k_B T} \left[\frac{\partial \ln(I(V))}{\partial V} \right], \tag{58}$$

in which $I(V)$ is the IV characteristic at a given temperature. Equation 58 can be derived from an approximation of Shockley diode equation, or by relating it to the differential conductance expression (starting from Shockley diode equation without approximation). However, both approaches are numerically equivalent and lead to Eq.58.

The application of Eq.58 to the experimental IV curves results in the ideality coefficients function of bias. An effective value for η has been extracted from each curve reported in Fig.26 considering a range of bias where curves show an exponential behavior.[133] Finally, extrapolated points have been reported in Fig.27.

The values of current and bias corresponding to each extrapolated η, reported in Fig.27, are consistent with the temperature dependency of threshold voltage and current, as reported in [129] and [1]. Furthermore, the values of η can be separated in two ranges, $1 \leqslant \eta \leqslant 2$ and $\eta > 2$, and each range can be related to a dominant transport mechanism. In case of $1 \leqslant \eta \leqslant 2$, the primary transport mechanism is a competition between drift-diffusion phenomena and Sah-Noyce-Shockley generation and recombination phenomena,[94] while for $\eta > 2$ the favoured transport mechanisms are trap-assisted tunneling (TAT) and carrier leakages.[34, 35, 82, 87] The dominant transport mechanism

can be deduced from Fig.27 is found to be TAT, in the range of temperatures below 200 K,[78, 81], while drift-diffusion is the favoured transport mechanisms for temperatures equal or above 200 K.
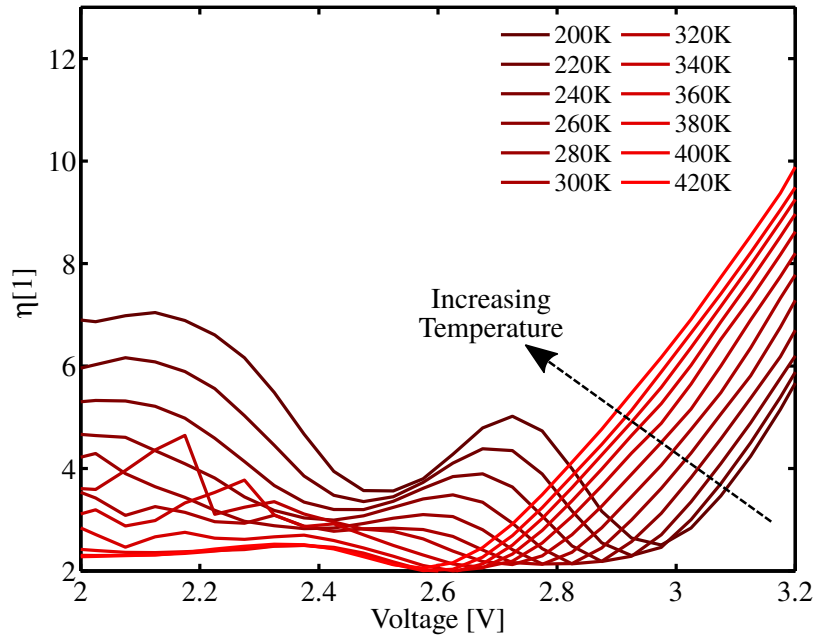

Figure 26: Ideality coefficient curves obtained from the application of Eq.58 to the experimental IV characteristics.

The analysis of the ideality coefficient allow to identify the range of temperatures and voltages at which experimental data can be correctly fitted by numerical simulations. Therefore, from results in Fig.27, numerical simulations are best suited to fit experimental data in the temperature range going from 200 K to 420 K and close to the voltage where the ideality coefficient reaches its minimum.

7.1.3 *Agreement with experimental IV characteristics*

In order to perform further studies on SRH recombinations, a preliminary agreement between simulated and measured IV characteristics (Fig.25) has to be achieved.

To each temperature, the measured IV characteristics have been fitted to the simulated IV curves by tuning two parameters: a serial resistor, and the amount of interface charge at the heterointerfaces, by tuning the α parameter in Eq.48. While the serial resistor account for a simple scaling factor, variations of the interface charge modify the built-in electric field. Therefore, different values of α impact on the threshold voltage, where flat-band condition is achieved.

Transient simulations have been carried out, at each temperature, by simulating the electrical behavior of circuit reported in Fig.28, for the device in forward bias conditions. Despite the range of valid temperatures determined through the ideality coefficient analysis, tem-
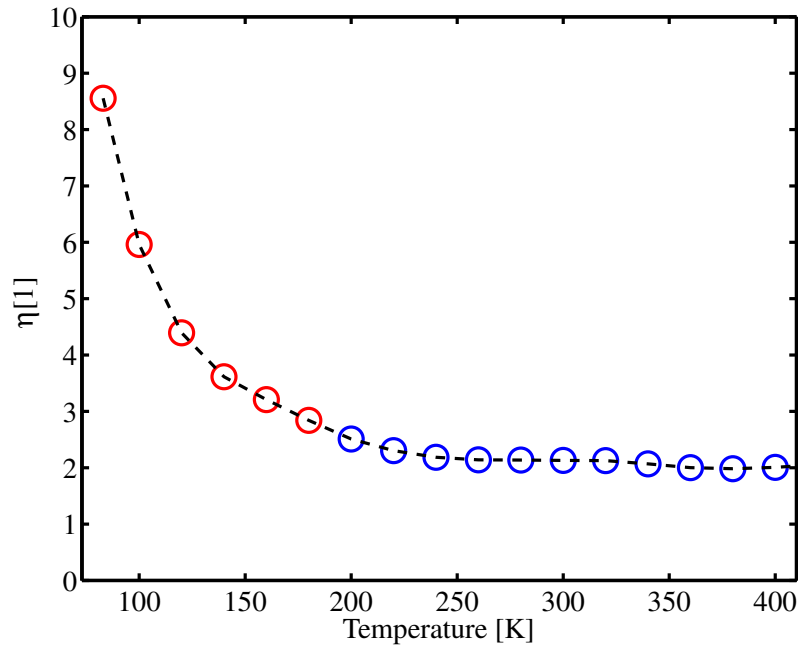
Figure 27: Minimum of ideality coefficient curves extrapolated in the exponential regime of IV curves. Red circles represent low temperature measurements representing signatures of TAT and carrier leakage as dominant transport mechanisms. Blue circles represent measurements in which drift-diffusion processes are supposed to be the dominant transport mechanism.

peratures ranging from 140 K to 420 K have been considered for fitting experimental IV characteristics. However, transient simulations didn't converge at temperatures lower than 140 K and the fit results to be accurate enough only for temperature equal or above 200 K.

Results for the fitting parameters R_C and α have been reported in Fig.30 and Fig.31. It can be noticed that above 200 K the contact resistance remains constant with temperature, while the interface charge coefficient increases linearly with temperature. Furthermore, the calculation of the ideality coefficient for the simulated IV characteristics, as expressed in Eq.58, reveal an ideality factor close to 1 for all temperatures. This fact verifies the nature of the dominant transport mechanism as a pure drift-diffusion process.

7.2 SIMULATIONS FOR THE THERMAL DROOP ANALYSIS

The thermal droop phenomena can be observed from experimental data on optical power reported in Fig.32. As can be seen from the normalized optical power curves reported in Fig.32, above a certain temperature the optically emitted power drastically drops by few orders of magnitude. Furthermore, together with the optical power measurements, the experimental τ_{SRH} function of temperature for the device has been measured, as reported in Fig.33.
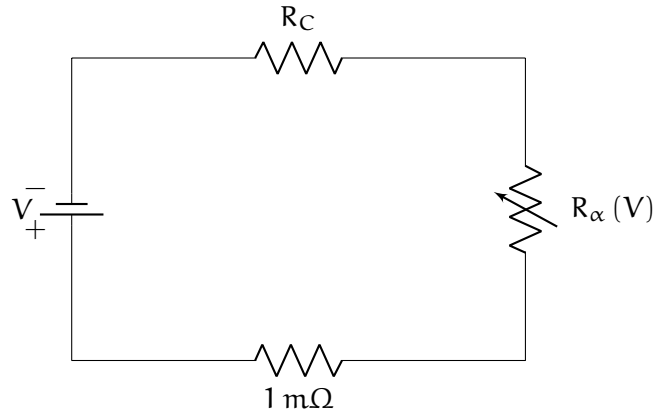
Figure 28: Equivalent simulation circuit in which R_C is the contact resistance, which has to be extrapolated from experimental data interpolation, and R_α (V) represent the device resistance for a given α. The device is modeled as a variable resistor function of the input voltage (V), as to reproduce the measured IV characteristic.
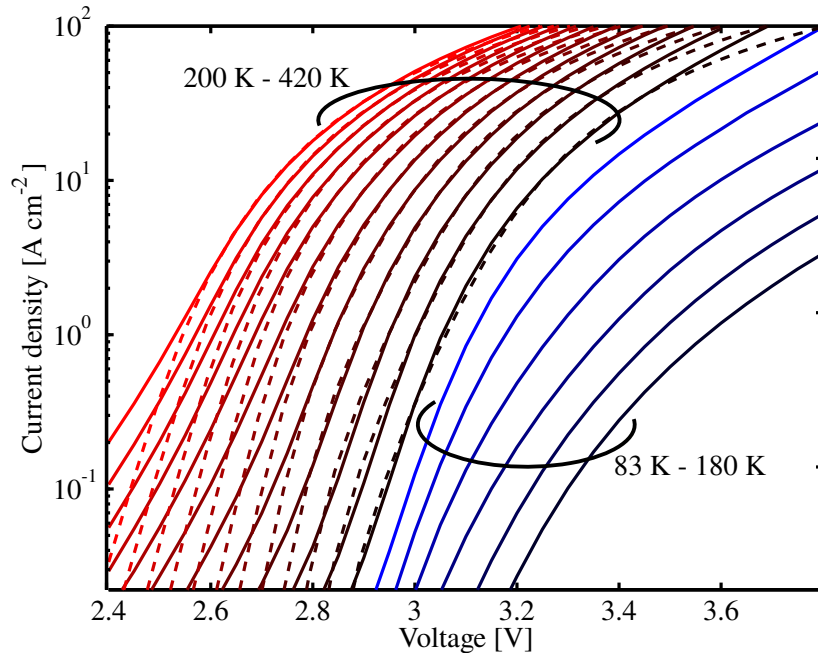
Figure 29: Semilogarithmic plot of experimental data on IV characteristics (solid lines), overlapped to simulated IV characteristics (dashed lines). Fitted curves have been reported starting from 200 K up to 420 K. Temperature of curves increases from right to left.

In order to asses the impact of SRH recombinations on the optically emitted power, three curves among those reported in Fig.32 have been considered as reference for comparison with numerical simulations. Thermal droop signatures are more pronounced at lower currents, where SRH processes are expected to be the dominant recombination mechanism. Therefore, curves at $0.2\,\mathrm{Acm^{-2}}$, $0.3\,\mathrm{Acm^{-2}}$, and
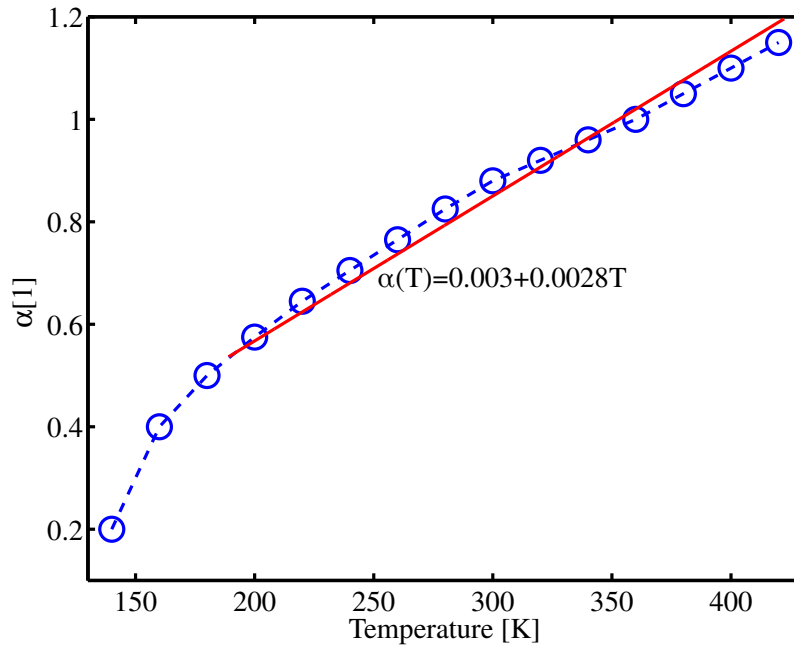
Figure 30: Values of α parameter, from Eq.48, used to fit experimental IV characteristics. The equation for α (T) refers to the red line, which represent the linear regression function of temperature for T above or equal to 200 K.
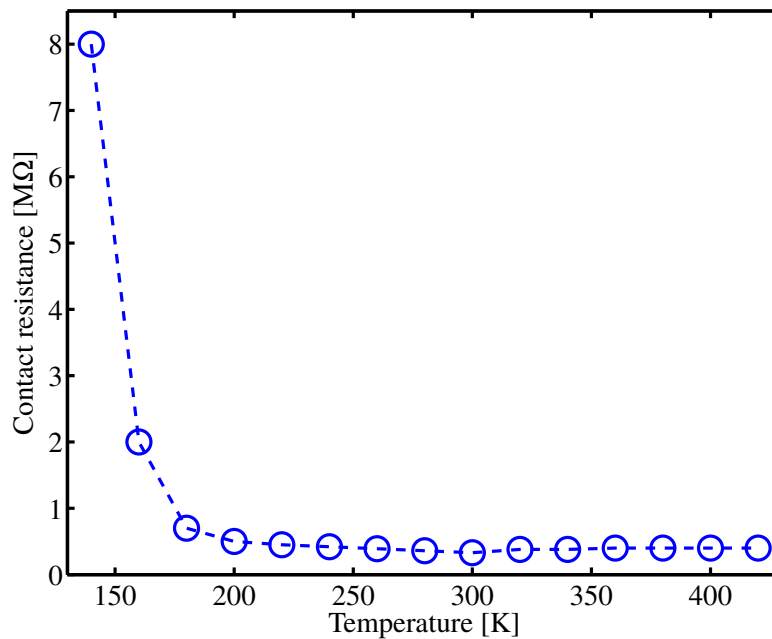
Figure 31: Values of R_C parameter used to fit experimental IV characteristics.

2.3 Acm^{-2} have been taken as reference for comparisons with numerical simulations.

Bearing in mind the established temperature limits, numerical simulations of current transitory have been performed for temperatures
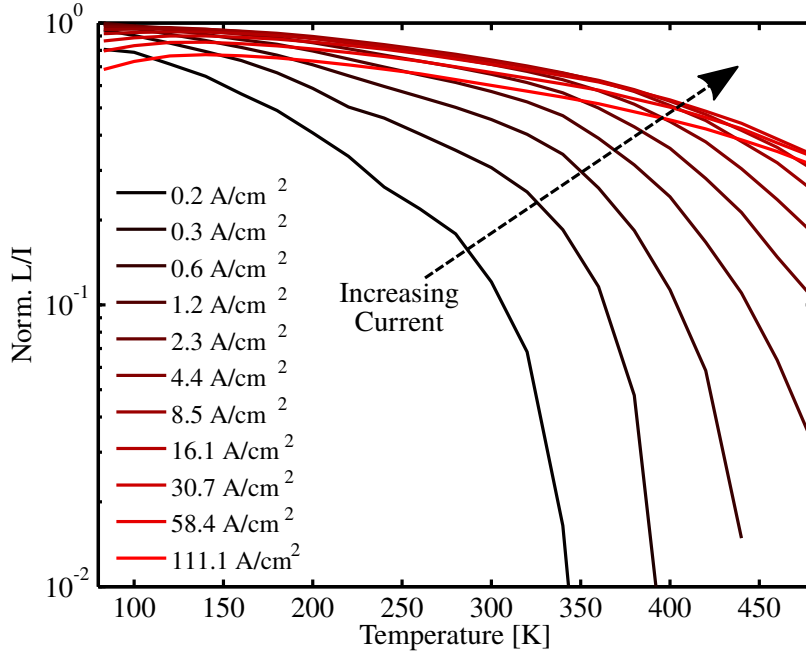
Figure 32: Experimental data on optically emitted power. Curves represent the ratio between the detected optical power and the injected current over a broad range of temperatures. The curves have been normalized with respect the maximum value for the entire set of data.
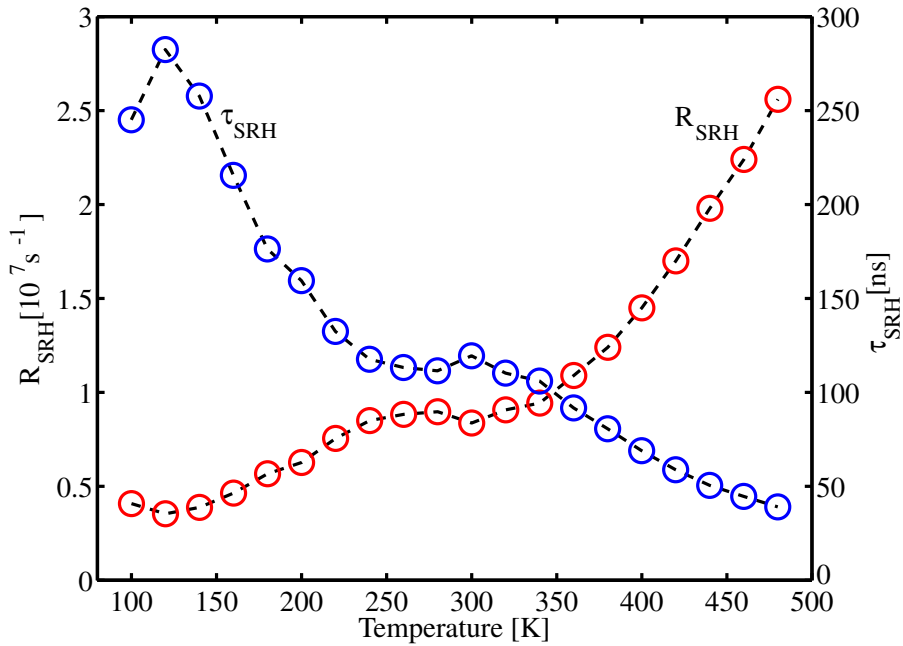
Figure 33: Experimental data on SRH recombination rate and the corresponding SRH lifetime function of temperature.

ranging from 140 K to 420 K. Once the ramped current density reached 0.2 Acm^{-2}, 0.3 Acm^{-2}, and 2.3 Acm^{-2}, output quantities, as the op-

tical power and the position dependent recombination rate profile along the device, were recorded.

7.2.1 *Further considerations on the SRH model*

The software Crosslight APSYS© implements Eq.55 to model the SRH recombination rate. If no trap concentration is specified, the software assumes a trap concentration equal to 1 cm^{-3} and computes the capture cross-section given the carrier lifetime and thermal velocities. However, trap states into the semiconductors are assumed to be fully activated and neutral. Therefore, the trap concentration does not take part to any other equation within the simulation flow (i.e. does not contribute to the electrostatic potential).

In spite of the trap concentration imposed by the software, the capture cross-section and trap concentration are two degrees of freedom of Eq.55. Moreover, the capture cross-section is usually considered a fitting parameter. Therefore, for a fixed carrier lifetime ($\tau_{n|p}$) and temperature, thermal velocities for electron and hole are fixed and all possible values of capture cross-section and trap concentration are represented by curves in Fig.34.
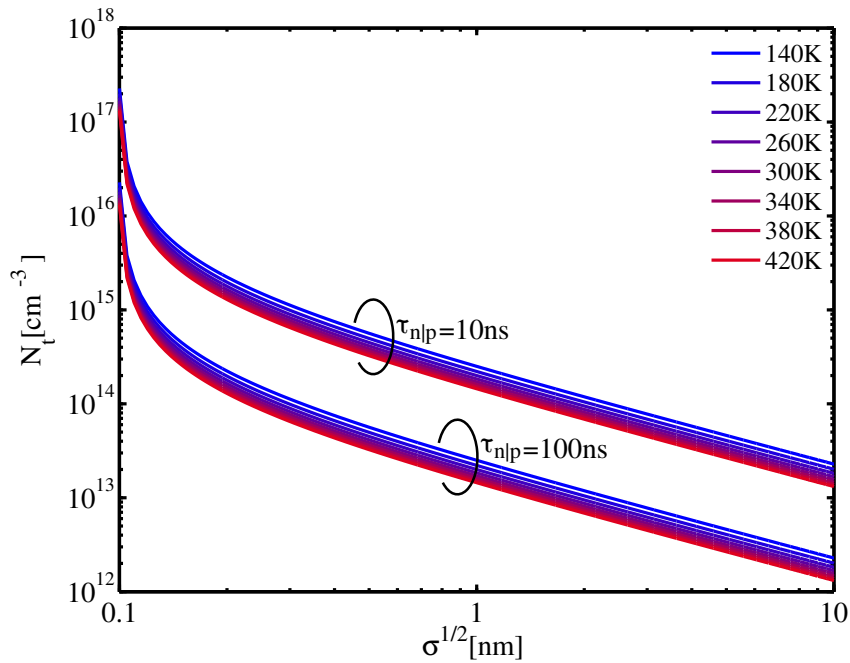

Figure 34: Logarithmic plot representing possible values of trap cross-section and trap concentration at different temperatures for a given carrier lifetime.

The electron and hole lifetime ($\tau_{n|p}$) given as parameters of SRH model represent different quantities from the experimentally measured SRH lifetime in Fig.33. Thus, in order to obtain an equivalent

SRH lifetime from simulation results, results from numerical simulation have been elaborated as follow.

A position dependent SRH coefficient have been calculated from the simulated carrier concentrations and SRH recombination rate as

$$A(x) = \frac{n(x) + p(x)}{n(x)\, p(x)} R_{SRH}(x),$$

(59)

then the position dependent SRH coefficient has been averaged over the quantum well profile according to

$$A = \frac{1}{L_{QW}} \int_{QW} A(x)\, dx.$$

(60)

From the equivalent SRH coefficient calculated in Eq.60, the SRH lifetime can be easily calculated as $\tau_{SRH} = 1/A$. This procedure has been performed for simulation results at all current and temperature points considered in this analysis.

7.3 RESULTS

The band diagram of the device, forwardly biased at 3 V, is reported in Fig.35. The image depict the conduction and valence band edge energies across the device active region, in a condition close to flat-band. Nonetheless, it is possible to observe a band bending in the quantum well that is opposite to the electric field direction due to the sheet charge layers at the GaN/InGaN heterointerfaces, induced by spontaneous polarization charge and lattice mismatch induced piezoelectric polarization charge. Furthermore, the layers reported in Fig.35 are in scale except for the n-GaN buffer, on the left side, and the p-GaN cap, on the right side, which have been truncated at the image frame.

From simulation results, the internal quantum efficiency (IQE), calculated as

$$IQE = \frac{R_{RAD}}{R_{SRH} + R_{RAD} + R_{AUG}},$$

(61)

has been compared to the normalized L/I curves extrapolated from experimental data.

The primary aim was to reproduce experimental results on τ_{SRH} and this goal has been achieved by imposing $\tau_n = \tau_p = 100$ ns. As reported in Fig.36, the simulated τ_{SRH} reproduce well the trend of experimental τ_{SRH}. However, the simulated IQE fails to reproduce the normalized L/I curves from experimental data, as reported in Fig.37.

The new values of τ_n and τ_p imposed for $In_{0.18}Ga_{0.82}N$ are one order of magnitude smaller with respect the ones reported in Tab.6. However, no sensible difference between the new and the old simulated IV characteristics has been observed. This is mainly due to
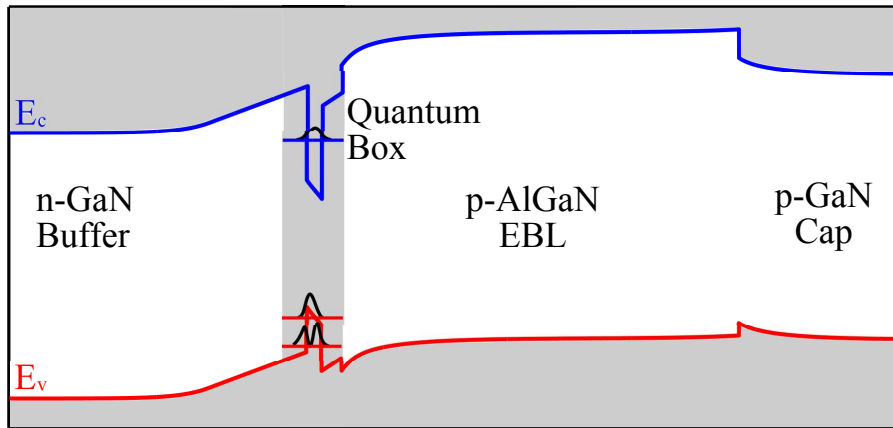
Figure 35: Conduction and valence band edge profiles across a portion of the device. The device has been forwardly biased at 3 V and the eigenfunctions resulting from **k·p** calculations in the quantum box have been reported. The framed portion of the device includes few nanometers of the *n*-GaN buffer on the left side and of the *p*-GaN cap layer on the right side.

the fact that the best fitting accuracy is achieved for current densities around $10\,\mathrm{Acm^{-2}}$, where SRH recombination play a minor role if compared to radiative and Auger processes.
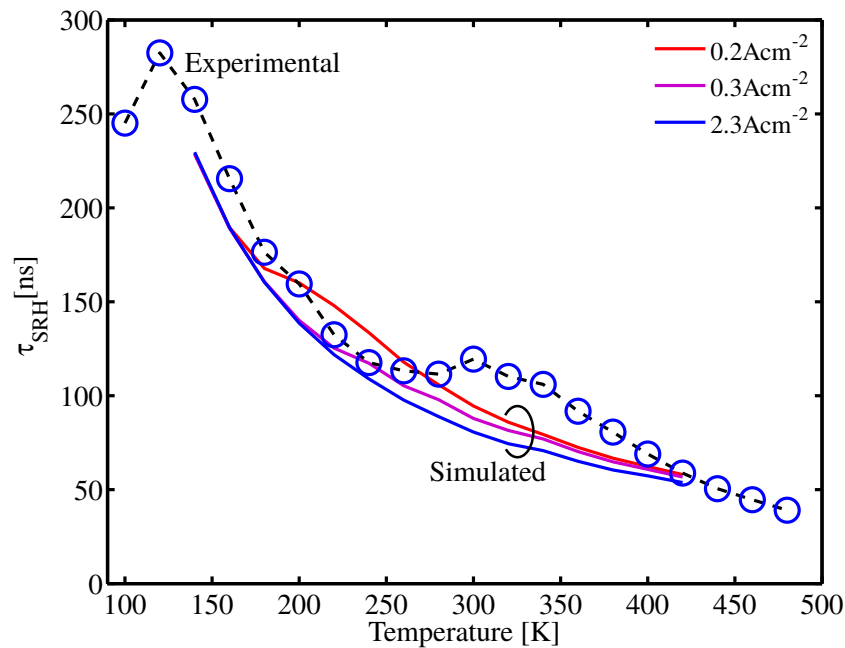
Figure 36: Simulated SRH lifetime (solid lines), calculated according to the procedure reported in Sec.7.2.1, compared to experimental SRH lifetime (circles over dashed line). The carrier lifetime ($\tau_{n|p}$) has been set to 100 ns for both electron and hole. This figure has been reported in the publication by De Santi *et al.*[43]
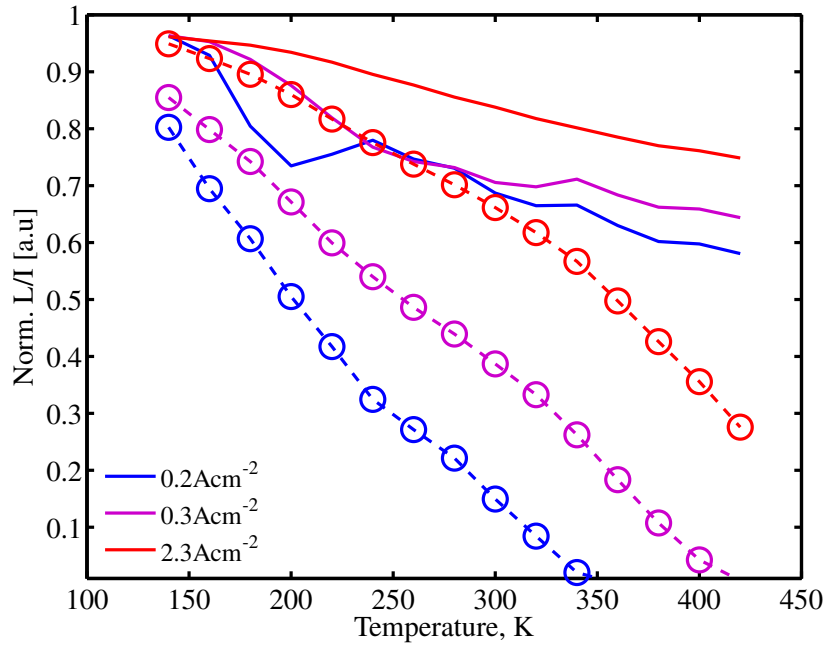
Figure 37: Comparison between the experimental normalized L/I curves (circles on dashed lines) and the simulated IQE (solid lines). In current simulations, τ_n and τ_p have been set to $100\,\text{ns}$. This figure has been reported in the publication by De Santi *et al.*[43]

Results reported in Fig.36 confirms that the temperature dependent model for the carrier lifetime (Eq.57) is able to reproduce the temperature dependency of SRH lifetime at all current points of interest. Furthermore, the formulation for the SRH recombination model, as reported in Eq.55 is independent from the trap concentration and capture cross-section, parameters that can be chosen to satisfy Eq.55 once the carrier lifetime has been provided, as depicted in Fig.34. Nonetheless, the inability to reproduce experimental data on the emitted optical power implies that the SRH recombination mechanisms cannot be ascribed as the primary cause to the thermal droop phenomena.

Parameter	GaN	InN	AlN	Units
a	3.1892	3.5446	4.982	Å
c	5.185	5.718	5.185	Å
E_g at $T = 0\,K$	3.507	0.735	6.23	eV
α	0.909	0.245	1.799	$meV\,K^{-1}$
β	830	624	1462	K
χ	4.07	5.9272	0.6	eV
Δ_{so}	14	1	-	meV
Δ_{cr}	19	41	-	meV
ε	9.5	15	8.5	-
$m_e^{\parallel}$	0.20	0.065	-	-
$m_e^{\perp}$	0.20	0.065	-	-
A_1	-6.56	-8.21	-	-
A_2	-0.91	-0.68	-	-
A_3	5.65	7.57	-	-
A_4	-2.83	-5.23	-	-
A_5	-3.13	-5.11	-	-
A_6	-4.86	-5.96	-	-
D_1	-3.0	-3.0	-	eV
D_2	3.6	3.6	-	eV
D_3	8.82	8.82	-	eV
D_4	-4.41	-4.41	-	eV
D_5	-4.0	-2.33	-	eV
D_6	-5.0770	-0.3536	-	eV
c_{11}	390	271	-	GPa
c_{12}	145	124	-	GPa
c_{13}	106	92	-	GPa
c_{33}	398	224	-	GPa
c_{44}	105	46	-	GPa
μ_n	300	300	300	$cm^2\,V^{-1}s^{-1}$
μ_p	10	10	10	$cm^2\,V^{-1}s^{-1}$
P^{SP}	-0.034	-0.090	-0.042	$10^{-4}C\,cm^{-2}$
P_b^{SP}	-	0.019	0.038	$10^{-4}C\,cm^{-2}$
$P^{(0)}$	-0.918	-1.808	-1.373	$10^{-4}C\,cm^{-2}$
$P^{(1)}$	9.541	5.624	7.599	$10^{-4}C\,cm^{-2}$

Table 5: Material parameters of GaN, InN, and AlN used in the present simulations. The quantum box is defined over the GaN/InGaN part of the active region. Therefore, no **k·p** parameters have been defined for AlN. The parameters for $In_{0.18}Ga_{0.82}N$ and $Al_{0.15}Ga_{0.85}N$ result from a linear interpolation of given values.

Parameter	GaN	$In_{0.18}Ga_{0.82}N$	$Al_{0.15}Ga_{0.85}N$	Units
m_e	0.2	0.188	0.2	-
m_h	1.5	1.67	1.09	-
ΔE_c	-	0.67	0.67	-
τ_n	$5 \cdot 10^{-8}$	$1.3 \cdot 10^{-6}$[97]	10^{-7}	s
τ_p	$5 \cdot 10^{-8}$	$1.3 \cdot 10^{-6}$[97]	10^{-7}	s
B	$2 \cdot 10^{-11}$	$1.13 \cdot 10^{-10}$[97]	$2 \cdot 10^{-11}$	$cm^3 s^{-1}$
C_n	$2.7 \cdot 10^{-30}$	$6.78 \cdot 10^{-32}$[97]	$2.7 \cdot 10^{-30}$	$cm^6 s^{-1}$
C_p	$2.7 \cdot 10^{-30}$	$6.78 \cdot 10^{-32}$[97]	$2.7 \cdot 10^{-30}$	$cm^6 s^{-1}$

Table 6: Table reporting the effective masses, band offset, SRH lifetimes, radiative recombination coefficients, and the Auger recombination coefficients used to obtain an agreement on experimental data.

8

Conclusions

In the second part of this work, the SRH recombination mechanism has been investigated as a possible source to the thermal droop problem in a GaN/InGaN based single quantum well light emitting diode. The electrical and the optical response of the device have been numerically simulated in Crosslight APSYS$^{©}$ by means of a drift-diffusion simulation scheme that has been locally coupled to the Schrödinger equation in the device active region.

The resolution of the Poisson's equation coupled to Schrödinger equation in the device active region, allowed to correctly describe the quantization phenomena taking place in the device active region. Furthermore, the resulting eigenfunctions have been used to compute the radiative recombination rate according to $\mathbf{k} \cdot \mathbf{p}$ theory.

A preliminary agreement between the experimental and simulated IV characteristics has been achieved for the device in forward bias conditions and over a broad range of temperatures. For each temperature, the fitting of an experimental IV curve took place by tuning two variables, a serial resistor and the coefficient of interface charge equation (Eq.48). While the serial resistor acts as a simple scaling factor, the interface charge coefficient is used to tune the threshold voltage. The best fit of experimental data has been obtained in the bias range where drift-diffusion phenomena are the primary transport mechanism. Furthermore, it has been verified by calculating the ideality coefficient of experimental curves and relating it to the dominant transport mechanism.

The SRH recombination processes have been studied as possible physical mechanism underlying the thermal droop phenomena. Given the experimentally measured SRH lifetime and optically emitted power function of temperature, a value for the carrier lifetime has been found such that the simulated SRH lifetime with temperature reproduces experimental data. However, the thermal droop signature observed in experimental data on emitted optical power could not be reproduced by numerical simulations. Therefore, it has been concluded that the SRH recombination mechanism alone cannot explain the thermal droop.

As part of the analysis on thermal droop phenomena, this work is part of the paper published by De Santi *et al.*[43]. The full study reported in [43] considers SRH recombinations and TAT as possible explanations to the thermal droop. However, the physics model proposed to fit experimental data describe an escape process character-

ized by thermionic emission aided by trap-assisted-tunneling of free carriers from the quantum well region to adjacent regions.

Bibliography

[1] HI Abdelkader, HH Hausien, and JD Martin. "Temperature rise and thermal rise-time measurements of a semiconductor laser diode." In: *Review of scientific instruments* 63.3 (1992), pp. 2004–2007. DOI: 10.1063/1.1143318.

[2] Hiroshi Amano, Masahiro Kito, Kazumasa Hiramatsu, and Isamu Akasaki. "P-type conduction in Mg-doped GaN treated with low-energy electron beam irradiation (LEEBI)." In: *Japanese Journal of Applied Physics* 28.12A (1989), p. L2112. DOI: 10.1143/JJAP.28.L2112.

[3] O Ambacher, B Foutz, J Smart, JR Shealy, NG Weimann, K Chu, M Murphy, AJ Sierakowski, WJ Schaff, LF Eastman, et al. "Two dimensional electron gases induced by spontaneous and piezoelectric polarization in undoped and doped AlGaN/GaN heterostructures." In: *Journal of Applied Physics* 87.1 (2000), pp. 334–344. DOI: http://dx.doi.org/10.1063/1.371866.

[4] Ashwin Ashok, Dragica Vasileska, Stephen M Goodnick, and Olin L Hartin. "Importance of the gate-dependent polarization charge on the operation of GaN HEMTs." In: *IEEE Transactions on Electron Devices* 56.5 (2009), pp. 998–1006. DOI: 10.1109/TED.2009.2015822.

[5] DH Auston, CV Shank, and P LeFur. "Picosecond optical measurements of band-to-band Auger recombination of high-density plasmas in germanium." In: *Physical Review Letters* 35.15 (1975), p. 1022. DOI: 10.1103/PhysRevLett.35.1022.

[6] Vitaliy Avrutin, Shopan A. Hafiz, Fan Zhang, Ümit Özgür, Enrico Bellotti, Francesco Bertazzi, Michele Goano, Arvydas Matulionis, Adam T. Roberts, Henry O. Everitt, and Hadis Morkoç. "Saga of efficiency degradation at high injection in InGaN light emitting diodes." In: *Turk. J. Phys.* 38.3 (Nov. 2014), pp. 269–313. DOI: 10.3906/fiz-1407-23.

[7] Sumith Bandara, Patrick Maloney, Neil Baril, Joseph Pellegrino, and Meimei Tidrow. "Performance of InAs/GaSb superlattice infrared detectors and dependence on minority carrier lifetime." In: *Infrared Physics & Technology* 54.3 (2011), pp. 263–266. DOI: 10.1016/j.infrared.2010.12.026.

[8] Randolph E Bank and Todd Dupont. "An optimal order process for solving finite element equations." In: *Mathematics of Computation* 36.153 (1981), pp. 35–51. DOI: 1981-36-153/S0025-5718-1981-0595040-2.

[9]   Randolph E Bank and Donald J Rose. "Parameter selection for Newton-like methods applicable to nonlinear partial differential equations." In: *SIAM Journal on Numerical Analysis* 17.6 (1980), pp. 806–822. DOI: 10.1137/0717068.

[10]   Randolph E Bank and Donald J Rose. "Global approximate Newton methods." In: *Numerische Mathematik* 37.2 (1981), pp. 279–295. DOI: 10.1007/BF01398257.

[11]   Randolph E Bank and Donald J Rose. "Analysis of a multilevel iterative method for nonlinear finite element equations." In: *Mathematics of Computation* 39.160 (1982), pp. 453–465. DOI: 1982-39-160/S0025-5718-1982-0669639-X.

[12]   W Bardyszewski and D Yevick. "Compositional dependence of the Auger coefficient for InGaAsP lattice matched to InP." In: *Journal of Applied Physics* 58.7 (1985), pp. 2713–2723. DOI: 10.1063/1.335909.

[13]   John J Barnes and Ronald J Lomax. "Finite-element methods in semiconductor device simulation." In: *IEEE Transactions on Electron Devices* 24 (1977), pp. 1082–1089. URL: http://adsabs.harvard.edu/abs/1977ITED...24.1082B.

[14]   M Bauer, J Taraci, J Tolle, AVG Chizmeshya, S Zollner, David J Smith, J Menendez, Changwu Hu, and J Kouvetakis. "Ge-Sn semiconductors for band-gap and lattice engineering." In: *Applied Physics Letters* 81.16 (2002), pp. 2992–2994. DOI: 10.1063/1.1515133.

[15]   Matthew R Bauer, John Tolle, Corey Bungay, Andrew VG Chizmeshya, David J Smith, José Menéndez, and John Kouvetakis. "Tunable band structure in diamond-cubic tin-germanium alloys grown on silicon substrates." In: *Solid State Communications* 127.5 (2003), pp. 355–359. DOI: 10.1016/S0038-1098(03)00446-0.

[16]   Daniel L. Becerra, Yuji Zhao, Sang Ho Oh, Christopher D. Pynn, Kenji Fujito, Steven P. DenBaars, and Shuji Nakamura. "High-power low-droop violet semipolar ($30\bar{3}\bar{1}$) InGaN/GaN light-emitting diodes with thick active layer design." In: *Applied Physics Letters* 105.17 (2014). DOI: 10.1063/1.4900793.

[17]   E. Bellotti, F. Bertazzi, S. Shishehchi, M. Matsubara, and M. Goano. "Theory of Carriers Transport in III-Nitride Materials: State of the Art and Future Outlook." In: *IEEE Trans. Electron Devices* 60.10 (Oct. 2013), pp. 3204–3215. DOI: 10.1109/TED.2013.2266577.

[18]   Fabio Bernardini, Vincenzo Fiorentini, and David Vanderbilt. "Spontaneous polarization and piezoelectric constants of III-V nitrides." In: *Physical Review B. Condensed Matter and Materi-*

als Physics 56.16 (1997), R10024. DOI: 10.1103/PhysRevB.56.R10024.

[19]   F. Bertazzi, M. Goano, and E. Bellotti. "A numerical study of Auger recombination in bulk InGaN." In: *Appl. Phys. Lett.* 97.23 (Dec. 2010), p. 231118. DOI: 10.1063/1.3525605.

[20]   F. Bertazzi, M. Goano, and E. Bellotti. "Calculation of Auger lifetime in HgCdTe." In: *Journal of Electronic Materials* 40.8 (2011), pp. 1663–1667. DOI: 10.1007/s11664-011-1638-5.

[21]   F. Bertazzi, M. Goano, and E. Bellotti. "Numerical analysis of indirect Auger transitions in InGaN." In: *Appl. Phys. Lett.* 101.1 (July 2012), p. 011111. DOI: 10.1063/1.4733353.

[22]   F. Bertazzi, S. Dominici, M. Mandurrino, D. Robidas, X. Zhou, M. Vallone, M. Calciati, P. Debernardi, G. Verzellesi, M. Meneghini, E. Bellotti, G. Ghione, and M. Goano. "Modeling challenges for high-efficiency visible light-emitting diodes." In: *Research and Technologies for Society and Industry Leveraging a better tomorrow (RTSI), 2015 IEEE 1st International Forum on*. 2015, pp. 157–160. DOI: 10.1109/RTSI.2015.7325090.

[23]   Francesco Bertazzi, Xiangyu Zhou, Michele Goano, Giovanni Ghione, and Enrico Bellotti. "Auger recombination in InGaN/GaN quantum wells. A full-Brillouin-zone study." In: *Appl. Phys. Lett.* 103.8 (Aug. 2013), p. 081106. DOI: 10.1063/1.4819129.

[24]   Francesco Bertazzi, Xiangyu Zhou, Michele Goano, Giovanni Ghione, and Enrico Bellotti. "Auger transitions and their signatures in III-nitride LEDs: a full-band modeling." In: *14th International Conference on Numerical Simulation of Optoelectronic Devices (NUSOD 2014)*. Palma de Mallorca, Spain, Sept. 2014, pp. 9–10. ISBN: 978-1-4799-3681-6. DOI: 10.1109/NUSOD.2014.6935330.

[25]   Francesco Bertazzi, Michele Goano, Marco Calciati, Xiangyu Zhou, Giovanni Ghione, and Enrico Bellotti. "Microscopic models of non-radiative and high-current effects in LEDs: state of the art and future developments." In: *SPIE Photonics West, Light-Emitting Diodes: Materials, Devices, and Applications for Solid State Lighting XVIII*. Ed. by Klaus P. Streubel, Heonsu Jeon, Li-Wei Tu, and Martin Strassburg. Vol. 9003, Proceedings of the SPIE. San Francisco, CA, Feb. 2014, pp. 900310–1–900310–7. DOI: 10.1117/12.2043234.

[26]   Francesco Bertazzi, Michele Goano, Xiangyu Zhou, Marco Calciati, Giovanni Ghione, Masahiko Matsubara, and Enrico Bellotti. "Looking for Auger signatures in III-nitride light emitters: A full-band Monte Carlo perspective." In: *Appl. Phys. Lett.* 106.6 (Feb. 2015), p. 061112. DOI: 10.1063/1.4908154.

[27] Francesco Bertazzi, Stefano Dominici, Marco Mandurrino, Dipika Robidas, Zhou Xiangyu, Marco Vallone, Marco Calciati, Pierluigi Debernardi, Giovanni Verzellesi, Matteo Meneghini, Enrico Bellotti, Giovanni Ghione, and Michele Goano. "Modeling challenges for high-efficiency visible light-emitting diodes." In: *International Forum on Research and Technologies for Society and Industry 2015 (RTSI 2015)*. Torino, Italy, Sept. 2015, pp. 157–160. DOI: `10.1109/RTSI.2015.7325090`.

[28] M. Binder, A. Nirschl, R. Zeisel, T. Hager, H.-J. Lugauer, M. Sabathil, D. Bougeard, J. Wagner, and B. Galler. "Identification of nnp and npp Auger recombination as significant contributor to the efficiency droop in (GaIn)N quantum wells by visualization of hot carriers in photoluminescence." In: *Applied Physics Letters* 103.7 (2013). DOI: `10.1063/1.4818761`.

[29] S Bloom and TK Bergstresser. "Band structure of α-Sn, InSb and CdTe including spin-orbit effects." In: *Solid State Communications* 6.7 (1968), pp. 465–467. DOI: `10.1016/0038-1098(68)90056-2`.

[30] P Boucaud, M El Kurdi, A Ghrib, M Prost, M de Kersauson, S Sauvage, F Aniel, X Checoury, G Beaudoin, L Largeau, et al. "Recent advances in germanium emission." In: *Photonics Research* 1.3 (2013), pp. 102–109. DOI: `0.1364/PRJ.1.000102`.

[31] C. Boztug, J. R. SanchezPerez, F. Cavallo, M. G. Lagally, and R. Paiella. "Strained-Germanium Nanostructures for Infrared Photonics." In: *ACS Nano* 8 (2014), pp. 3136–3151. DOI: `10.1021/nn404739b`.

[32] J. Bude, K. Hess, and G. J. Iafrate. "Impact ionization in semiconductors: Effects of high electric fields and high scattering rates." In: *Phys. Rev. B* 45.19 (May 1992), pp. 10958–10964.

[33] Marco Calciati, Michele Goano, Francesco Bertazzi, Marco Vallone, Xiangyu Zhou, Giovanni Ghione, Matteo Meneghini, Gaudenzio Meneghesso, Enrico Zanoni, Enrico Bellotti, Giovanni Verzellesi, Dandan Zhu, and Colin Humphreys. "Correlating electroluminescence characterization and physics-based models of InGaN/GaN LEDs: Pitfalls and open issues." In: *AIP Adv.* 4.6 (June 2014), p. 067118. DOI: `10.1063/1.4882176`.

[34] XA Cao, EB Stokes, PM Sandvik, SF LeBoeuf, J Kretchmer, and D Walker. "Diffusion and tunneling currents in GaN/InGaN multiple quantum well light-emitting diodes." In: *IEEE Electron Device Letters* 23.9 (2002), pp. 535–537. DOI: `10.1109/LED.2002.802601`.

[35] HC Casey Jr, J Muth, S Krishnankutty, and JM Zavada. "Dominance of tunneling current and band filling in InGaN/AlGaN double heterostructure blue light-emitting diodes." In: *Applied*

Physics Letters 68.20 (1996), pp. 2867–2869. DOI: `10.1063/1.116351`.

[36] AVG Chizmeshya, C Ritter, J Tolle, C Cook, J Menendez, and J Kouvetakis. "Fundamental studies of P (GeH$_3$) $_3$, As (GeH$_3$) $_3$, and Sb (GeH$_3$)$_3$: Practical n-dopants for new group IV semiconductors." In: *Chemistry of Materials* 18.26 (2006), pp. 6266–6277. DOI: `10.1021/cm061696j`.

[37] S. L. Chuang and C. S. Chang. "k · p method for strained wurtzite semiconductors." In: *Phys. Rev. B* 54.4 (July 1996), pp. 2491–2504. DOI: `10.1103/PhysRevB.54.2491`.

[38] Shun Lien Chuang. "Optical gain of strained wurtzite GaN quantum-well lasers." In: *IEEE Journal of quantum Electronics* 32.10 (1996), pp. 1791–1800. DOI: `10.1109/3.538786`.

[39] Enrico Clementi and Carla Roetti. "Roothaan-Hartree-Fock atomic wavefunctions: Basis functions and their coefficients for ground and certain excited states of neutral and ionized atoms, Z ⩽ 54." In: *Atomic data and nuclear data tables* 14.3 (1974), pp. 177–478. DOI: `10.1016/S0092-640X(74)80016-1`.

[40] MARVIN Cohen and James R Chelikowsky. *Electronic structure and optical properties of semiconductors*. Vol. 75. Springer Science & Business Media, 2012.

[41] Marvin L Cohen, James R Chelikowsky, and Jurgen R Meyer-Arendt. "Electronic Structure and Optical Properties of Semiconductors." In: *Applied Optics* 28 (1989), p. 2388.

[42] *Crosslight Device Simulation Software - General Manual*. ©1995-2013 Crosslight Software Inc.

[43] C. De Santi, M. Meneghini, M. La Grassa, B. Galler, R. Zeisel, M. Goano, S. Dominici, M. Mandurrino, F. Bertazzi, D. Robidas, G. Meneghesso, and E. Zanoni. "Role of defects in the thermal droop of InGaN-based light emitting diodes." In: *Journal of Applied Physics* 119.9 (2016). DOI: `10.1063/1.4942438`.

[44] Stefano Dominici, Hanqing Wen, Francesco Bertazzi, Michele Goano, and Enrico Bellotti. "Numerical evaluation of Auger recombination coefficients in relaxed and strained germanium." In: *Applied Physics Letters* 108.21 (May 2016), p. 211103. DOI: `10.1063/1.4952720`.

[45] Stefano Dominici, Hanqing Wen, Francesco Bertazzi, Michele Goano, and Enrico Bellotti. "Numerical study on the optical and carrier recombination processes in GeSn alloy for E-SWIR and MWIR optoelectronic applications." In: *Optics Express* 24.23 (2016), pp. 26363–26381. DOI: `10.1364/OE.24.026363`.

[46] Wei Du, Yiyin Zhou, Seyed A Ghetmiri, Aboozar Mosleh, Benjamin R Conley, Amjad Nazzal, Richard A Soref, Greg Sun, John Tolle, Joe Margetis, et al. "Room-temperature electroluminescence from $Ge/Ge_{1-x}Sn_x/Ge$ diodes on Si substrates." In: *Applied Physics Letters* 104.24 (2014), p. 241110. DOI: 10.1063/1.4884380.

[47] Wei Du, Yiyin Zhou, Seyed A Ghetmiri, Aboozar Mosleh, Benjamin R Conley, Amjad Nazzal, Richard A Soref, Greg Sun, John Tolle, Joe Margetis, et al. "Room-temperature electroluminescence from $Ge/Ge_{1-x}Sn_x/Ge$ diodes on Si substrates." In: *Applied Physics Letters* 104.24 (2014), p. 241110. DOI: 10.1063/1.4884380.

[48] Vincenzo Fiorentini, Fabio Bernardini, and Oliver Ambacher. "Evidence for nonlinear macroscopic polarization in III–V nitride alloy heterostructures." In: *Applied Physics Letters* 80.7 (2002), pp. 1204–1206. DOI: 10.1063/1.1448668.

[49] M. V. Fischetti and S. E. Laux. "Band structure, deformation potentials, and carrier mobility in strained Si, Ge, and SiGe alloys." In: *Journal of Applied Physics* 80.4 (Aug. 1996), pp. 2234–2252.

[50] FL Freitas, J Furthmüller, F Bechstedt, M Marques, and LK Teles. "Influence of the composition fluctuations and decomposition on the tunable direct gap and oscillator strength of $Ge_{1-x}Sn_x$ alloys." In: *Applied Physics Letters* 108.9 (2016), p. 092101. DOI: 10.1063/1.4942971.

[51] M. Goano, F. Bertazzi, M. Penna, and E. Bellotti. "Electronic structure of wurtzite ZnO: Nonlocal pseudopotential and *ab initio* calculations." In: *J. Appl. Phys.* 102.8 (2007), p. 083709. DOI: 10.1063/1.2794380.

[52] CHL Goodman. "Device Applications of Direct Gap Group IV Semiconductors." In: *Japanese Journal of Applied Physics* 22.S1 (1983), p. 583. DOI: 10.7567/JJAPS.22S1.583.

[53] W. Grieshaber, E. F. Schubert, I. D. Goepfert, R. F. Karlicek, M. J. Schurman, and C. Tran. "Competition between band gap and yellow luminescence in GaN and its relevance for optoelectronic devices." In: *Journal of Applied Physics* 80.8 (1996), pp. 4615–4620. DOI: http://dx.doi.org/10.1063/1.363443.

[54] H. K. Gummel. "A Self-Consistent Iterative Scheme for One-Dimensional Steady State Transistor Calculations." In: *IEEE Trans. Electron Devices* ED-11 (Oct. 1964), pp. 455–465.

[55] Jay Prakash Gupta, Nupur Bhargava, Sangcheol Kim, Thomas Adam, and James Kolodzey. "Infrared electroluminescence from GeSn heterojunction diodes grown by molecular beam epi-

taxy." In: *Applied Physics Letters* 102.25 (2013), p. 251117. DOI: 10.1063/1.4812747.

[56]   A Haug. "Phonon-assisted auger recombination in degenerate semiconductors." In: *Solid State Communications* 22.8 (1977), pp. 537–539. DOI: 10.1016/0038-1098(77)91409-0.

[57]   A Haug. "Auger recombination of electron-hole drops." In: *Solid State Communications* 25.7 (1978), pp. 477–479. DOI: 10.1016/0038-1098(78)90161-8.

[58]   Gang He and Harry A Atwater. "Interband transitions in Sn_xGe_{1-x} alloys." In: *Physical Review Letters* 79.10 (1997), p. 1937. DOI: 10.1103/PhysRevLett.79.1937.

[59]   Frank Herman, Charles D Kuglin, Kermit F Cuff, and Richard L Kortum. "Relativistic corrections to the band structure of tetrahedrally bonded semiconductors." In: *Physical Review Letters* 11.12 (1963), p. 541. DOI: 10.1103/PhysRevLett.11.541.

[60]   Chul Huh and Seong-Ju Park. "Effects of temperature on InGaN/GaN LEDs with different MQW structures." In: *Electrochemical and solid-state letters* 7.11 (2004), G266–G268. DOI: 1099-0062/2004/7(11)/G266/3/.

[61]   L. Huldt. "Auger recombination in germanium." In: *Physica Status Solidi A* 24.1 (1974), pp. 221–229. DOI: 10.1002/pssa.2210240119.

[62]   L Huldt. "Phonon-assisted Auger recombination in germanium." In: *Physica Status Solidi A* 33.2 (1976), pp. 607–614. DOI: 10.1002/pssa.2210330220.

[63]   Justin Iveland, Lucio Martinelli, Jacques Peretti, James S. Speck, and Claude Weisbuch. "Direct Measurement of Auger Electrons Emitted from a Semiconductor Light-Emitting Diode under Electrical Injection: Identification of the Dominant Mechanism for Efficiency Droop." In: *Physical Review Letters* 110 (17 2013), p. 177406. DOI: 10.1103/PhysRevLett.110.177406.

[64]   Radi A Jishi. *Feynman diagram techniques in condensed matter physics*. Cambridge University Press, 2013.

[65]   P. D. C. King, T. D. Veal, and C. F. McConville. "Nonparabolic coupled Poisson-Schrödinger solutions for quantized electron accumulation layers: Band bending, charge profile, and subbands at InN surfaces." In: *Physical Review B. Condensed Matter and Materials Physics* 77 (12 2008), p. 125305. DOI: 10.1103/PhysRevB.77.125305.

[66]   Kazuhide Kumakura, Toshiki Makimoto, and Naoki Kobayashi. "Mg-acceptor activation mechanism and transport characteristics in p-type InGaN grown by metalorganic vapor phase epitaxy." In: *Journal of Applied Physics* 93.6 (2003), pp. 3370–3375. DOI: http://dx.doi.org/10.1063/1.1545155.

[67]   PT Landsberg and MJ Adams. "Radiative and Auger processes in semiconductors." In: *Journal of Luminescence* 7 (1973), pp. 3–34. DOI: 10.1016/0022-2313(73)90057-4.

[68]   P.T. Landsberg and A.R. Beattie. "Auger effect in semiconductors." In: *Journal of Physics and Chemistry of Solids* 8 (1959), pp. 73–75. DOI: 10.1016/0022-3697(59)90276-8.

[69]   HK Lee, JS Yu, and YT Lee. "Thermal analysis and characterization of the effect of substrate thinning on the peformances of GaN-based light emitting diodes." In: *Physica Status Solidi A* 207.6 (2010), pp. 1497–1504. DOI: 10.1002/pssa.200925575.

[70]   Seong Jae Lee, Tae Song Kwon, Kyun Nahm, and Chul Koo Kim. "Band structure of ternary compound semiconductors beyond the virtual crystal approximation." In: *Journal of Physics: Condensed Matter* 2.14 (1990), p. 3253. DOI: 10.1088/0953-8984/2/14/010.

[71]   G. Lehmann and M. Taut. "On the Numerical Calculation of the Density of States and Related Properties." In: *Physica Status Solidi B* 54.2 (1972), pp. 469–477. ISSN: 1521-3951. DOI: 10.1002/pssb.2220540211.

[72]   M. Leroux, N. Grandjean, M. Laügt, J. Massies, B. Gil, P. Lefebvre, and P. Bigenwald. "Quantum confined Stark effect due to built-in internal polarization fields in (Al,Ga)N/GaN quantum wells." In: *Physical Review B. Condensed Matter and Materials Physics* 58 (20 1998), R13371–R13374. DOI: 10.1103/PhysRevB.58.R13371.

[73]   C. K. Li and Y. R. Wu. "Study on the Current Spreading Effect and Light Extraction Enhancement of Vertical GaN/InGaN LEDs." In: *IEEE Transactions on Electron Devices* 59.2 (2012), pp. 400–407. ISSN: 0018-9383. DOI: 10.1109/TED.2011.2176132.

[74]   W Lochmann and A Haug. "Phonon-assisted Auger recombination in Si with direct calculation of the overlap integrals." In: *Solid State Communications* 35.7 (1980), pp. 553–556. DOI: 10.1016/0038-1098(80)90896-0.

[75]   C. Lombardi, S. Manzini, A. Saporito, and M. Vanzi. "A physically based mobility model for numerical simulation of nonplanar devices." In: *IEEE Transactions on Computer-Aided Design of Integrated Circuits and Systems* 7.11 (1988), pp. 1164–1171. DOI: 10.1109/43.9186.

[76]   James H. Luscombe, Ann M. Bouchard, and Marshall Luban. "Electron confinement in quantum nanostructures: Self-consistent Poisson-Schrödinger theory." In: *Physical Review B. Condensed Matter and Materials Physics* 46 (16 1992), pp. 10262–10268. DOI: 10.1103/PhysRevB.46.10262.

[77] Gerald D Mahan. *Many-particle physics*. Springer Science & Business Media, 2013.

[78] Marco Mandurrino, Giovanni Verzellesi, Michele Goano, Marco Vallone, Francesco Bertazzi, Giovanni Ghione, Matteo Meneghini, Gaudenzio Meneghesso, and Enrico Zanoni. "Trap-assisted tunneling in InGaN/GaN LEDs: experiments and physics-based simulation." In: *14th International Conference on Numerical Simulation of Optoelectronic Devices (NUSOD 2014)*. Palma de Mallorca, Spain, Sept. 2014, pp. 13–14. ISBN: 978-1-4799-3681-6. DOI: 10.1109/NUSOD.2014.6935332.

[79] Marco Mandurrino, Giovanni Verzellesi, Michele Goano, Marco Vallone, Francesco Bertazzi, Giovanni Ghione, Matteo Meneghini, Gaudenzio Meneghesso, and Enrico Zanoni. "Physics-based modeling and experimental implications of trap-assisted tunneling in InGaN/GaN light-emitting diodes." In: *Phys. Status Solidi A* 212.5 (2015), pp. 947–953. DOI: 10.1002/pssa.201431743.

[80] Marco Mandurrino, Michele Goano, Marco Vallone, Francesco Bertazzi, Giovanni Ghione, Giovanni Verzellesi, Matteo Meneghini, Gaudenzio Meneghesso, and Enrico Zanoni. "Semiclassical simulation of trap-assisted tunneling in GaN-based light-emitting diodes." In: *J. Comp. Electron.* 14.2 (June 2015), pp. 444–455. DOI: 10.1007/s10825-015-0675-3.

[81] Marco Mandurrino, Michele Goano, Stefano Dominici, Marco Vallone, Francesco Bertazzi, Giovanni Ghione, Mario Bernabei, Luigi Rovati, Giovanni Verzellesi, Matteo Meneghini, Gaudenzio Meneghesso, and Enrico Zanoni. "Trap-assisted tunneling contributions to subthreshold forward current in InGaN/GaN light-emitting diodes." In: *SPIE Optics+Photonics, 14th International Conference on Solid State Lighting and LED-based Illumination Systems*. Vol. 9571, Proceedings of the SPIE. San Diego, CA, Aug. 2015, 95710U–1–95710U–6. DOI: 10.1117/12.2187443.

[82] K Mayes, A Yasan, R McClintock, D Shiell, SR Darvish, P Kung, and M Razeghi. "High-power 280 nm AlGaN light-emitting diodes based on an asymmetric single-quantum well." In: *Applied Physics Letters* 84.7 (2004), pp. 1046–1048. DOI: 10.1063/1.1647273.

[83] David S. Meyaard, Qifeng Shan, Jaehee Cho, E. Fred Schubert, Sang-Heon Han, Min-Ho Kim, Cheolsoo Sone, Seung Jae Oh, and Jong Kyu Kim. "Temperature dependent efficiency droop in GaInN light-emitting diodes with different current densities." In: *Applied Physics Letters* 100.8 (2012). DOI: 10.1063/1.3688041.

[84] Pairot Moontragoon, Zoran Ikonić, and Paul Harrison. "Band structure calculations of Si–Ge–Sn alloys: achieving direct band gap materials." In: *Semiconductor Science and Technology* 22.7 (2007), p. 742. DOI: 10.1088/0268-1242.

[85] Shuji Nakamura, Takashi Mukai, and Masayuki Senoh. "High-brightness InGaN/AlGaN double-heterostructure blue-green-light-emitting diodes." In: *Journal of Applied Physics* 76.12 (1994), pp. 8189–8191. DOI: 10.1063/1.357872.

[86] Madelung Otfried. *Semiconductors: data handbook*. Springer-Verlag, 2004.

[87] Piotr Perlin, Marek Osiński, Petr G Eliseev, Vladimir A Smagley, Jian Mu, Michael Banas, and Philippe Sartori. "Low-temperature study of current and electroluminescence in InGaN/AlGaN/-GaN double-heterostructure blue light-emitting diodes." In: *Applied physics letters* 69.12 (1996), pp. 1680–1682. DOI: 10.1063/1.117026.

[88] Benjamin Pinkie and Enrico Bellotti. "Numerical simulation of spatial and spectral crosstalk in two-color MWIR/LWIR HgCdTe infrared detector arrays." In: *Journal of Electronic Materials* 42.11 (2013), pp. 3080–3089. DOI: 10.1007/s11664-013-2647-3.

[89] W. Porod and D. K. Ferry. "Modification of the virtual-crystal approximation for ternary III-V compounds." In: *Physical Review B. Condensed Matter and Materials Physics* 27 (4 1983), pp. 2587–2589. DOI: 10.1103/PhysRevB.27.2587.

[90] CV Ramakrishnan. "An upwind finite element scheme for the unsteady convective diffusive transport equation." In: *Applied Mathematical Modelling* 3.4 (1979), pp. 280–284. DOI: 10.1016/S0307-904X(79)80059-1.

[91] M. A. Reshchikov, D. O. Demchenko, A. Usikov, H. Helava, and Yu. Makarov. "Carbon defects as sources of the green and yellow luminescence bands in undoped GaN." In: *Physical Review B. Condensed Matter and Materials Physics* 90 (23 2014), p. 235203. DOI: 10.1103/PhysRevB.90.235203.

[92] Michael A. Reshchikov and Hadis Morkoç. "Luminescence properties of defects in GaN." In: *Journal of Applied Physics* 97.6 (2005). DOI: http://dx.doi.org/10.1063/1.1868059.

[93] Friedhard Römer and Bernd Witzigmann. "Acceptor activation model for III-nitride LEDs." In: *Journal of Computational Electronics* 14.2 (2015), pp. 456–463. DOI: 10.1007/s10825-015-0666-4.

[94] Chih-Tang Sah, Robert N Noyce, and William Shockley. "Carrier generation and recombination in pn junctions and pn junction characteristics." In: *Proceedings of the IRE* 45.9 (1957), pp. 1228–1243. DOI: 10.1109/JRPROC.1957.278528.

[95] D. L. Scharfetter and H. K. Gummel. "Large-Signal Analysis of a Silicon Read Diode Transistor." In: *IEEE Trans. Electron Devices* ED-16.1 (Jan. 1969), pp. 64–77.

[96] A Schenk. "A model for the field and temperature dependence of Shockley-Read-Hall lifetimes in silicon." In: *Solid-State Electronics* 35.11 (1992), pp. 1585–1596. DOI: 10.1016/0038-1101(92)90184-E.

[97] Dario Schiavon, Michael Binder, Matthias Peter, Bastian Galler, Philipp Drechsel, and Ferdinand Scholz. "Wavelength-dependent determination of the recombination rate coefficients in single-quantum-well GaInN/GaN light emitting diodes." In: *Physica Status Solidi B* 250.2 (2013), pp. 283–290. ISSN: 1521-3951. DOI: 10.1002/pssb.201248286.

[98] Siegfried Selberherr. *Analysis and simulation of semiconductor devices*. Springer Science & Business Media, 2012.

[99] CL Senaratne, PM Wallace, JD Gallagher, PE Sims, John Kouvetakis, and Jose Menendez. "Direct gap $Ge_{1-y}Sn_y$ alloys: Fabrication and design of mid-IR photodiodes." In: *Journal of Applied Physics* 120.2 (2016), p. 025701. DOI: 10.1063/1.4956439.

[100] Y. C. Shen, G. O. Mueller, S. Watanabe, N. F. Gardner, A. Munkholm, and M. R. Krames. "Auger recombination in InGaN measured by photoluminescence." In: *Applied Physics Letters* 91.14 (2007). DOI: 10.1063/1.2785135.

[101] W. Shockley and W. T. Read. "Statistics of the Recombinations of Holes and Electrons." In: *Physical Review B. Condensed Matter and Materials Physics* 87 (5 1952), pp. 835–842. DOI: 10.1103/PhysRev.87.835.

[102] Richard Soref, Joshua Hendrickson, and Justin W. Cleary. "Mid- to long-wavelength infrared plasmonic-photonics using heavily doped n-Ge/Ge and n-GeSn/GeSn heterostructures." In: *Optics Express* 20.4 (2012), pp. 3814–3824. DOI: 10.1364/OE.20.003814.

[103] EH Steenbergen, BC Connelly, GD Metcalfe, H Shen, M Wraback, D Lubyshev, Y Qiu, JM Fastenau, AWK Liu, S Elhamri, et al. "Significantly improved minority carrier lifetime observed in a long-wavelength infrared III-V type-II superlattice comprised of InAs/InAsSb." In: *Applied Physics Letters* 99.25 (2011), p. 251110. DOI: 10.1063/1.3671398.

[104] MJ Süess, R Geiger, RA Minamisawa, G Schiefler, J Frigerio, D Chrastina, G Isella, R Spolenak, J Faist, and H Sigg. "Analysis of enhanced light emission from highly strained germanium microbridges." In: *Nature Photonics* 7.6 (2013), pp. 466–472. DOI: 10.1038/nphoton.2013.67.

[105] David S Sukhdeo, Donguk Nam, Ju-Hyung Kang, Mark L Brongersma, and Krishna C Saraswat. "Direct bandgap germanium-on-silicon inferred from 5.7% $\langle 100 \rangle$ uniaxial tensile strain." In: *Photonics Research* 2.3 (2014), A8–A13. DOI: 10.1364/PRJ.2.0000A8.

[106] Simon M Sze and Kwok K Ng. *Physics of semiconductor devices*. John wiley & sons, 2006.

[107] Masumi Takeshima. "Green's-function formalism of band-to-band Auger recombination in semiconductors. Correlation effect." In: *Physical Review B. Condensed Matter and Materials Physics* 26.2 (1982), p. 917. DOI: 10.1103/PhysRevB.26.917.

[108] Masumi Takeshima. "Unified theory of the impurity and phonon scattering effects on Auger recombination in semiconductors." In: *Physical Review B. Condensed Matter and Materials Physics* 25.8 (1982), p. 5390. DOI: 10.1103/PhysRevB.25.5390.

[109] Masumi Takeshima. "Intervalence-Band Absorption in Relation to Auger Recombination in Laser Materials." In: *Japanese Journal of Applied Physics* 23.4R (1984), p. 428. URL: http://stacks.iop.org/1347-4065/23/i=4R/a=428.

[110] Alexander A Tonkikh, Christian Eisenschmidt, Vadim G Talalaev, Nikolay D Zakharov, Joerg Schilling, Georg Schmidt, and Peter Werner. "Pseudomorphic GeSn/Ge (001) quantum wells: Examining indirect band gap bowing." In: *Applied Physics Letters* 103.3 (2013), p. 032106. DOI: 10.1063/1.4813913.

[111] Huong Tran, Wei Du, Seyed A Ghetmiri, Aboozar Mosleh, Greg Sun, Richard A Soref, Joe Margetis, John Tolle, Baohua Li, Hameed A Naseem, et al. "Systematic study of $Ge_{1-x}Sn_x$ absorption coefficient and refractive index for the device applications of Si-based optoelectronics." In: *Journal of Applied Physics* 119.10 (2016), p. 103106. DOI: 10.1063/1.4943652.

[112] A. Trellakis, A. T. Galick, A. Pacelli, and U. Ravaioli. "Iteration scheme for the solution of the two-dimensional Schrödinger-Poisson equations in quantum structures." In: *J. Appl. Phys.* 81.12 (June 1997), pp. 7880–7884.

[113] Marco Vallone, Marco Mandurrino, Michele Goano, Francesco Bertazzi, Giovanni Ghione, Wilhelm Schirmacher, Stefan Hanna, and Heinrich Figgemeier. "Numerical Modeling of SRH and Tunneling Mechanisms in High-Operating-Temperature MWIR

HgCdTe Photodetectors." In: *Journal of Electronic Materials* 44.9 (2015), pp. 3056–3063. DOI: 10.1007/s11664-015-3767-8.

[114] Yatendra Pal Varshni. "Temperature dependence of the energy gap in semiconductors." In: *Physica* 34.1 (1967), pp. 149–154. DOI: 10.1016/0031-8914(67)90062-6.

[115] Giovanni Verzellesi, Davide Saguatti, Matteo Meneghini, Francesco Bertazzi, Michele Goano, Gaudenzio Meneghesso, and Enrico Zanoni. "Efficiency droop in InGaN/GaN blue light-emitting diodes: Physical mechanisms and remedies." In: *J. Appl. Phys.* 114.7 (Aug. 2013), p. 071101. DOI: 10.1063/1.4816434.

[116] M Virgilio, CL Manganelli, G Grosso, G Pizzi, and G Capellini. "Radiative recombination and optical gain spectra in biaxially strained n-type germanium." In: *Physical Review B. Condensed Matter and Materials Physics* 87.23 (2013), p. 235313. DOI: 10.1103/PhysRevB.87.235313.

[117] J. P. Walter and M. L. Cohen. "Frequency- and Wave-Vector-Dependent Dielectric Function for Silicon." In: *Physical Review B. Condensed Matter and Materials Physics* 5.8 (Apr. 1972), pp. 3101–3110.

[118] John P Walter, Marvin L Cohen, Y Petroff, and M Balkanski. "Calculated and measured reflectivity of ZnTe and ZnSe." In: *Physical Review B* 1.6 (1970), p. 2661. DOI: 10.1103/PhysRevB.2.2268.3.

[119] Pei Wang, Wei Wei, Bin Cao, Zhiyin Gan, and Sheng Liu. "Simulation of current spreading for GaN-based light-emitting diodes." In: *Optics & Laser Technology* 42.5 (2010), pp. 737–740. DOI: 10.1016/j.optlastec.2009.11.018.

[120] Zhong Lin Wang, Xiang Yang Kong, Yong Ding, Puxian Gao, William L Hughes, Rusen Yang, and Yue Zhang. "Semiconducting and piezoelectric oxide nanostructures induced by polar surfaces." In: *Advanced Functional Materials* 14.10 (2004), pp. 943–956. DOI: 10.1002/adfm.200400180.

[121] Gideon Weisz. "Band structure and Fermi surface of white tin." In: *Physical Review* 149.2 (1966), p. 504. DOI: 10.1103/PhysRev.149.504.

[122] Hanqing Wen. "Advanced numerical modeling of semiconductor material properties and their device performances." PhD thesis. Boston University, 2016. URL: http://hdl.handle.net/2144/17068.

[123] Hanqing Wen and Enrico Bellotti. "Numerical Analysis of Radiative Recombination in Narrow-Gap Semiconductors Using the Green's Function Formalism." In: *Journal of Electronic Materials* 43.8 (2014), pp. 2841–2848. DOI: 10.1007/s11664-014-3123-4.

[124] Hanqing Wen and Enrico Bellotti. "Optical absorption and intrinsic recombination in relaxed and strained $InAs_{1-x}Sb_x$ alloys for mid-wavelength infrared application." In: *Applied Physics Letters* 107.22 (2015), p. 222103. DOI: 10.1063/1.4936862.

[125] Hanqing Wen and Enrico Bellotti. "Rigorous theory of the radiative and gain characteristics of silicon and germanium lasing media." In: *Physical Review B. Condensed Matter and Materials Physics* 91.3 (2015), p. 035307. DOI: 10.1103/PhysRevB.91.035307.

[126] Hanqing Wen, Benjamin Pinkie, and Enrico Bellotti. "Direct and phonon-assisted indirect Auger and radiative recombination lifetime in HgCdTe, InAsSb, and InGaAs computed using Green's function formalism." In: *Journal of Applied Physics* 118.1 (2015), p. 015702. DOI: 10.1063/1.4923059.

[127] S Wirths, D Buca, and S Mantl. "Si–Ge–Sn alloys: From growth to applications." In: *Progress in Crystal Growth and Characterization of Materials* 62.1 (2016), pp. 1–39. DOI: 10.1016/j.pcrysgrow.2015.11.001.

[128] S Wirths, R Geiger, N von den Driesch, G Mussler, T Stoica, S Mantl, Z Ikonic, M Luysberg, S Chiussi, JM Hartmann, et al. "Lasing in direct-bandgap GeSn alloy grown on Si." In: *Nature Photonics* 9.2 (2015), pp. 88–92. DOI: 10.1038/nphoton.2014.321.

[129] Y Xi and EF Schubert. "Junction-temperature measurement in GaN ultraviolet light-emitting diodes using diode forward voltage method." In: *Applied Physics Letters* 85.12 (2004), pp. 2163–2165. DOI: 10.1063/1.1795351.

[130] Junqi Xie, J Tolle, VR D'Costa, C Weng, AVG Chizmeshya, Jose Menendez, and John Kouvetakis. "Molecular approaches to p- and n-nanoscale doping of $Ge_{1-y}Sn_y$ semiconductors: Structural, electrical and transport properties." In: *Semiconductor Science and Technology* 53.8 (2009), pp. 816–823. DOI: 10.1016/j.sse.2009.04.013.

[131] Kyounghoon Yang, Jack R East, and George I Haddad. "Numerical modeling of abrupt heterojunctions using a thermionic-field emission boundary condition." In: *Solid-State Electronics* 36.3 (1993), pp. 321–330. DOI: 10.1016/0038-1101(93)90083-3.

[132] Yiyin Zhou, Wei Dou, Wei Du, Thach Pham, Seyed Amir Ghetmiri, Sattar Al-Kabi, Aboozar Mosleh, Murtadha Alher, Joe Margetis, John Tolle, et al. "Systematic study of GeSn heterostructure-based light-emitting diodes towards mid-infrared applications." In: *Journal of Applied Physics* 120.2 (2016), p. 023102. DOI: 10.1063/1.4958337.

[133]   Di Zhu, Jiuru Xu, Ahmed N Noemaun, Jong Kyu Kim, E Fred Schubert, Mary H Crawford, and Daniel D Koleske. "The origin of the high diode-ideality factors in GaInN/GaN multiple quantum well light-emitting diodes." In: *Applied Physics Letters* 94.8 (2009), p. 081113. DOI: 10.1063/1.3089687.